Meteorology And Atmospheric Physics
June 2023, Volume 135 Issue 3 Pages 29 (22p.)
https://doi.org/10.1007/s00703-023-00967-0
https://archimer.ifremer.fr/doc/00836/94764/

Comparing GlobCurrent dataset with numerical results from a high-resolution implementation of the POLCOMS-WAM coupled system under a strong gap wind over the Gulf of Tehuantepec

Larranaga Marco [1,], Osuna Pedro [2], Esquivel-Trava Bernardo [2], Ocampo-Torres Francisco J. [3], Rascle Nicolas [4], Garcia-Nava Hector [5], Moulin Aimie [6]

[1] LEGOS, Universiteé de Toulouse, IRD, CNRS, CNES, UPS, Toulouse, France
[2] Departamento de Oceanografía Física, CICESE, Ensenada, Baja California, México
[3] CEMIE-Océano, Instituto de Ingeniería, UNAM, Ciudad de México, México
[4] LOPS, CNRS, Ifremer, IRD, University of Brest, Brest, France
[5] Instituto de Investigaciones Oceanológicas, UABC, Ensenada, Baja California, México
[6] Ocean modeling and Data Assimilation, CMCC, Bologna, Italy

* Corresponding author : Marco Larranaga, email address : marco.larranaga@legos.obs-mip.fr

osunac@cicese.mx ; esquivel@cicese.mx ; pocampotorres@gmail.com ; nicolas.rascle@ifremer.fr ; hector.gnava@uabc.edu.mx ; aimie.moulin@cmcc.it

Abstract :

GlobCurrent provides a variety of datasets aiming to describe global ocean circulation, especially when dealing with large-scale phenomena. It includes surface Stokes drift and geostrophic, Ekman, and total (geostrophic plus Ekman) currents. GlobCurrent uses the CNES-CLS13 mean dynamic topography estimation as well as data from sea surface drifters and wind reanalysis to improve the computation of ocean currents from altimetry data, which represents a significant advance in describing the total ocean current. The aim of this work is to compare the surface GlobCurrent estimates with a coupled ocean–wave numerical simulation (POLCOMS-WAM), drifting buoys, and altimeter observations when dealing with a Tehuano event, i.e., intense (larger than 20 m s −1) and short duration (around 3–5 days) low-level winds blowing over the Gulf of Tehuantepec, Mexico. There is a good agreement between the wind-driven currents (Ekman currents plus Stokes drift) field from GlobCurrent and that estimated by POLCOMS–WAM, with the largest magnitudes ∼0.8 m s−1 in the region influenced by the highest winds' speed. The geostrophic circulation patterns in the Gulf of Tehuantepec are similarly reproduced by GlobCurrent and POLCOMS-WAM. However, some differences were observed in the presence of an anticyclonic eddy located in the western part of the study area. Numerical results exhibit a more symmetrical eddy with geostrophic current speeds that, in agreement with along-track observations, exceed the 1 m s−1. Instead, the geostrophic eddy in GlobCurrent shows velocities of about 0.8 m s−1. As observed through drifting buoys in 2000, numerical results show that the anticyclonic eddy west of the GoT has strong ageostrophic currents related to a cyclogeostrophic balance, which is not included in GlobCurrent. This

regional case study provides a guideline for future improvements of GlobCurrent products, in particular for the estimation of geostrophic and total currents.

1 Introduction

One of the greatest challenges faced by the scientific community is to obtain reliable estimates of sea surface currents around the world, either through observations or numerical simulations. Realistic estimates of surface currents are a fundamental tool for the improvement of fisheries, monitoring of plastics and oil spills, development and operation of offshore structures, and even estimating the drift of search and rescue objects. The first ocean current global records were estimated from historical ship drifts and hydrographic data (Arnault, 1987; Richardson, 1989; Reverdin et al., 1994), with large space and time gaps in the data set (Cheney et al., 1983). With the rise of satellite observations, several studies were focused on reconstructing the sea surface currents from satellite altimetry and surface wind fields. This idea is based on the Ralph and Niiler (1999) work, in which it is mentioned that ∼80% of the ocean currents variance can be explained through the linear combination of geostrophic and Ekman currents. Lagerloef et al. (1999) obtained the first surface current speed estimate from satellite–derived sea surface height and wind stress, as well

as drifters data via a physically-based statistical model. Further ahead, the OSCAR (Ocean Surface Currents Analysis Real Time; Bonjean and Lagerloef, 2002) and GECKO (Geostrophic and Ekman Current Observatory; Sudre et al., 2013) products distributed sea surface current speed estimations, where geostrophic currents are computed from the absolute dynamic topography,*i.e.,* altimeter sea level anomalies (SLA) plus a mean dynamic topography (MDT) estimation, and the Ekman currents from the SSMI (Special Sensor Microwave Imager; Atlas et al., 1996). The main differences between both products are related to the treatment of currents near the equator. Nevertheless, several works (Maximenko and Niiler, 2006; Bakun, 2006; Penven et al., 2014; Douglass and Richman, 2015) have shown that in the presence of strong mesoscale eddies or current meanders, the geostrophic balance is no longer valid since the centrifugal acceleration could be important, leading these structures to be in cyclogeostrophic balance. Not including a cyclogeostrophic correction results in an underestimation (overestimation) of the current velocities in mesoscale eddies/meanders with negative (positive) vorticity (Maximenko and Niiler, 2006; Penven et al., 2014).

The GlobCurrent project has been funded by the European Space Agency's Earth Observation Envelope Programme, aiming to develop an operational system to provide ocean currents data derived from a combination of remote sensing, in-situ, and numerical model data. The GlobCurrent data repository includes geostrophic and Stokes-drift currents at the surface, and Ekman and total currents at the surface and 15 m depth. The main improvement in GlobCurrent with other products lies in using the CNES–CLS13 MDT (Mean Dynamic Topography; Rio et al., 2014) to calculate geostrophic currents. Besides, GlobCurrent uses the synergy between a set of surface drifters and atmospheric reanalysis data to estimate an empirical Ekman model that can reproduce an Ekman–like spiral (Rio et al., 2014).

Diverse studies have aimed to validate the GlobCurrent dataset in order to propose improvements in the methodology to compute the dynamic variables. Feng et al. (2018) evaluate the surface GlobCurrent products in the Northwestern Atlantic (Mid–Atlantic Bight and the Gulf of Maine) using current profilers and high–frequency radars. The authors suggest that a refinement of the mean dynamic topography could better represent the ocean dynamics near the coast. Cancet et al. (2019) employed current profilers and drifting buoys in order to assess the performance of GlobCurrent products in two regions of Australia: the South–East, principally forced by the East Australian Current, and the Joseph Bonaparte Gulf, forced by tides and wind–driven currents. Their study states that GlobCurrent does not properly solve the dynamics of the continental shelf due to the coarse resolution of the MDT and satellite altimetry. Besides, the authors suggest that it is important to add a tidal–current component in order to obtain more accurate estimates of total currents in tidally–dominated regions.

The aim of this work is to analyse the capability of the GlobCurrent dataset to reproduce the mesoscale ocean dynamics generated by strong mountain

gap–winds (low—level winds that blow through a gap between mountains) forcing in the Gulf of Tehuantepec (GoT), Mexico. Mountain gap–winds are defined as jets of air that result from the combination of large–scale synoptic forcing and the configuration of local topography. The analysis is carried out by comparing the GlobCurrent dataset with the available observations and results from a high–resolution numerical implementation of a 3D model that includes wave–current interactions.

This paper is organized as follows. Section 2 includes a brief description of the study region, whereas Section 3 describes the data used in this study and details of the coupled model implementation. From Section 6 to section 7, the GlobCurrent products (Stokes drift and geostrophic, Ekman, and total currents) are compared with observations and the numerical model results. Finally, the conclusions are presented in section 8.

2 The Gulf of Tehuantepec

The Isthmus of Tehuantepec (Fig. 1), located in the southeast of Mexico, extends from 93 to 96°W and from 15 to 16°N. It is a narrow region of the Sierra Madre del Sur that separates the Pacific Ocean from the Gulf of Mexico. In this region, the mountain range is about 2000 m above the mean sea level and in the central part of the isthmus it breaks down into a broad plateau–like ridge. The mean terrain altitude drastically drops to about 250 m, forming a gap of approximately 40 km width known as Chivela pass. Mainly during the winter season, the combination of atmospheric pressure differences between the Gulf of Mexico and the Gulf of Tehuantepec, as well as this orographic feature, produce strong gap–winds that can reach speeds higher than 20 m s^{-1} known as Tehuanos or Tehuntepecers (Barton et al., 1993; Romero-Centeno et al., 2003). This characteristic wind field spreads south–southwestward hundreds of kilometers over the Pacific Ocean and can last from a few hours to several days.

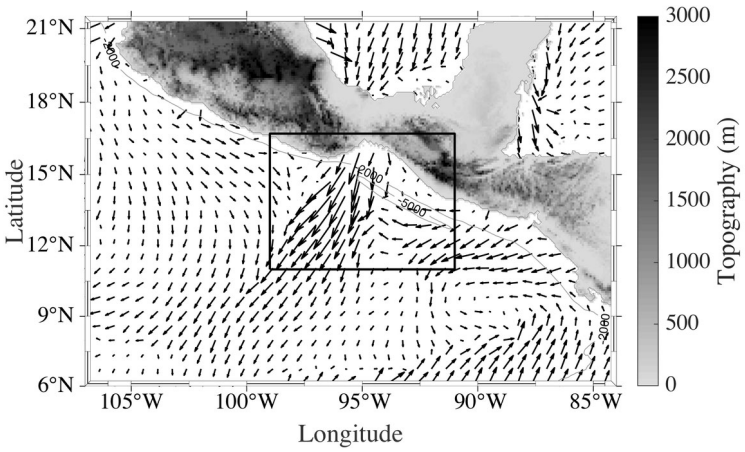

Fig. 1: Typical wind field in the Gulf of Tehuantepec under the presence of a Tehuano event, as reproduced by the WRF model. The 2000 and 5000 m contours of the ocean bathymetry are included. The black arrows indicate wind vectors and the inner frame represents the area where the ocean dynamics are analyzed.

The ocean response under these winds produces southward currents that favor an intense upwelling. This condition promotes the transport of colder water to the surface and generates a mesoscale asymmetric dipolar current field (Barton et al., 1993; Trasviña et al., 1995; Amador et al., 2006; Santiago-García et al., 2019). The mechanism of this asymmetric circulation pattern could be explained by the gap–winds Ekman pumping, which produces a convergence (divergence) to the right (left) along the region influenced by a Tehuano event, and a downwelling (upwelling) that generate an anticyclonic (cyclonic) eddy (Willett et al., 2006). Anticyclonic and cyclonic eddies are likely to be propagated from the coast to the southwest and west, and anticyclonic eddies are more common, larger, and intense compared with cyclonic ones (Müller-Karger and Fuentes-Yaco, 2000; Palacios and Bograd, 2005). However, other phenomena involved in the generation of eddies in the Gulf of Tehuantepec are instabilities triggered by the mean flow (Liang et al., 2012) or by the propagation of Kelvin waves along the coast (Zamudio et al., 2006). On the other hand, Trasviña and Barton (2008) found that an anticyclonic eddy generated by gap–winds in the Gulf of Tehuantepec continuously change its propagation speeds by the influence of subsequent gap–wind events, confirming that the direct action of gap–winds can induce important modifications in eddies properties.

With regard to the sea state, in the Gulf of Tehuantepec the presence of swell from the southern Pacific Ocean is persistent during most of the year, but during a Tehuano event, fetch–limited wave growth occurs and wind–waves propagate in opposite direction to the incoming swell (Ocampo-Torres et al., 2010).

This study focuses on examining the response of ocean dynamics to the most intense Tehuano event (northerly winds) during October 2010, which occurs between the 13th and 19th of this month. Time series of wind and wave parameters in a point located at the central part of the Gulf of Tehuantepec, approximately 22 km offshore, are shown in Fig. 2, where can be observed that the Tehuano reached, at that point, wind speeds of about 20 ms^{-1} (top panel), producing waves with a significant height up to 5 m (bottom panel).

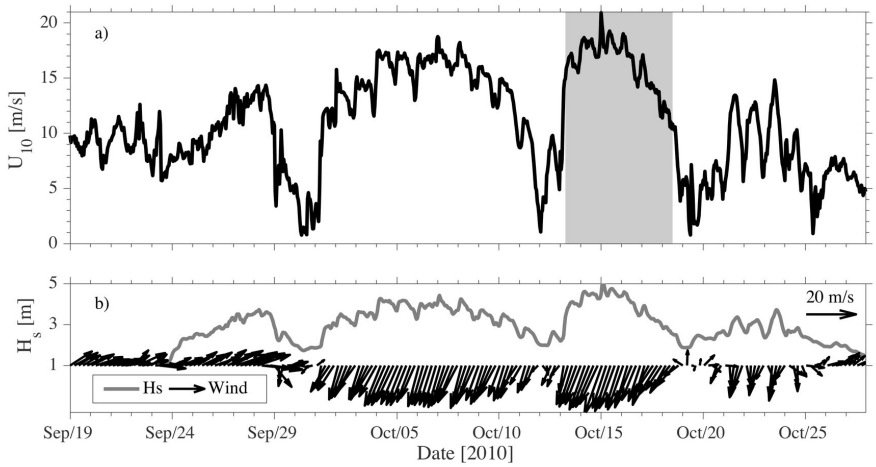

Fig. 2: Time series of wind and wave parameters (from WRF and POLCOMS–WAM, respectively) at position (95.46W,14.93N). The wind speed is shown in panel (a) and wind vectors and significant wave height are shown in panel (b). The gray–shaded area corresponds to the Tehuano event selected for the analysis.

3 Data

3.1 GlobCurrent dataset

This study makes use of the surface GlobCurrent v2 dataset, which is composed of: geostrophic currents, Ekman currents, total currents (the linear combination of geostrophic and Ekman currents), and the Stokes drift. GlobCurrent geostrophic velocity is calculated from a combination of altimetry, gravimetry, and *in situ* data. Their improvement in the computation of geostrophic currents is the use of a global CNES–CLS13 MDT generated by Rio et al. (2014). The CNES–CLS13 MDT is the result of the synergy of multiple datasets, such as Ssalto/Duacs delayed–time maps of altimeter height and geostrophic velocity anomalies distributed by the Copernicus Marine Environment Monitoring Service (CMEMS), an altimeter mean sea surface from Schaeffer et al. (2012) and the latest version of a geoid model data from Bruinsma et al. (2013). The *in*

situ data is composed of the Coriolis Ocean database ReAnalysis (CORA3.4), the Yoshinari Maximenko Hacker (YoMaHa'07) dataset, and the Surface Velocity Program data distributed by the Surface Drifter Data Assembly Center (SD–DAC). In addition, wind stress data from ERA–interim reanalysis is used.

In order to compute the CNES–CLS13 MDT, Rio et al. (2014) first calculate the geodetic MDT by subtracting the geoid model from the mean sea surface, and after that, an optimal filter is applied. The calculation of MDT is improved by estimating the mean heights and mean geostrophic velocities from surface buoy data. This is accomplished by removing the variability of sea surface height and geostrophic currents from altimeter data, as well as empirical surface Ekman currents and wind slippage from the undrogued drifters (Rio et al., 2014). A low-pass filter is applied to the processed drifter data in order to eliminate remaining ageostrophic currents, such as inertial oscillations and tides. Finally, the geostrophic currents are calculated from the gradient of the absolute dynamic topography, h, which is obtained as the sum of the CMEMS sea level anomaly and the CNES–CLS13 MDT, to be subsequently merged into a homogeneous grid.

The computation of the GlobCurrent Ekman currents is based on the model proposed by Rio and Hernandez (2003); Rio (2012) and Rio et al. (2014), which consist in a two–parameter ($\beta(z)$, $\theta(z)$) approximation:

$$\mathbf{u}_{ek}(z) = \beta(z)\boldsymbol{\tau} e^{i\theta(z)}, \tag{1}$$

where the $\beta(z)$ and $\theta(z)$ parameters correspond to the amplitude factor and the phase difference between ageostrophic currents and wind stress, respectively. These parameters are computed by applying the least squares fit between the ERA-Interim wind stress ($\boldsymbol{\tau}$) and ageostrophic buoy currents. In order to consider spatial and temporal variations of $\beta(z)$ and $\theta(z)$, these parameters are calculated in monthly windows and domains of $4^\circ \times 4^\circ$ degrees. Ageostrophic buoy currents at the surface are obtained by extracting geostrophic currents from ARGO floats, where geostrophic currents are estimated using the absolute dynamic topography from altimetry. Ageostrophic currents are mainly composed of Ekman currents, but also by the contribution of inertial oscillations and the Stokes–drift (Rio et al., 2014). In agreement with Lewis and Belcher (2004), Rio et al. (2014) mention that by including the Stokes drift into the Ekman current estimation, current deflections from 10° to 45° between the surface currents and the wind stress are obtained. Since Ekman currents, inertial oscillations, and the Stokes drift of locally generated waves depend on the wind, we will refer to these as wind–driven currents.

Moreover, total currents in GlobCurrent are reconstructed as a linear combination of the geostrophic and the wind–driven current ($\mathbf{u} = \mathbf{u}_{geo} + \mathbf{u}_{wd}$).

Regarding Stokes drift, this is a mass–transport velocity in the direction of wave propagation occurring since individual particles in a progressive irrotational wave do not exactly describe closed paths (Longuet-Higgins, 1953). Stokes drift velocity decays rapidly away from the surface, over a length scale

known as the Stokes depth. In GlobCurrent the Stokes drift product is based on the theoretical derivation by Huang (1971), and it is calculated using the third moment of wave spectrum obtained from the global WAVEWATCH III® model, as follows:

$$U_s = \iint 2\omega k S(\omega, k) e^{2|k|z} dk d\omega, \tag{2}$$

where $S(\omega, k)$ is the directional wave energy spectrum. The contribution from the high frequencies of the spectrum is included according to Rascle and Ardhuin (2013). It is worth noting that although wave–current interactions effects are not commonly important in open waters (Bolaños et al., 2011), these can modulate sea surface waves in regions with strong boundary currents (Abolfazli et al., 2020; Wang et al., 2020; Allahdadi et al., 2022; de León and Soares, 2022), and the wave model used to estimate the Stokes drift in GlobCurrent does not include the effects of surface currents on the evolution of the wave spectra (Ardhuin et al., 2012).

3.2 CMEMS altimetry

This study makes use of sea surface height and geostrophic currents gridded provided by the Copernicus Marine Environment Monitoring Service CMEMS (2017), with daily temporal resolution and 1/4° horizontal resolution.

3.3 Satellite altimetry along–track sea level anomaly

Along–track sea level anomaly data from the Center of Topography of the Ocean and Hydrosphere (CTOH; Birol et al., 2017) in Toulouse can be used to compute geostrophic currents with higher accuracy. The X–TRACK processing tool v2.0 from CTOH allows geophysical corrections for removing the aliasing of tides and short-term atmospheric effects in the measurements. Following Birol and Delebecque (2014), a low–pass filter with a 35–km cut–off is applied to the along–track CTOH sea level anomaly in order to remove measurement noise. Along–track altimeter has a sampling resolution of 1–Hz, allowing estimations of sea level anomalies with a spatial resolution of about 1.3 km in the GoT.

3.4 Mean dynamic topography

Besides employing the CNES–CLS13 MDT, this work analyzes the performance of a new MDT in the computation of geostrophic currents in the GoT, the CNES–CLS18. A detailed description of the CNES–CLS18 product, as well as the considerations of its development can be found in Mulet et al. (2021).

3.5 Drifting buoys

Standard surface drifters of the Tropical Ocean and Global Atmosphere–World Ocean Circulation Experiment (TOGA–WOCE; Lumpkin and Pazos, 2007) are used in this study to describe surface the GoT surface dynamics during Tehuano events in June 2000 (Trasviña and Barton, 2008).

3.6 The POLCOMS–WAM coupled system

The POLCOMS (Proudman Oceanographic Laboratory Coastal Ocean Modelling System; Holt and James, 2001) is a tridimensional baroclinic B–grid model that solves the hydrostatic, incompressible (Boussinesq) equations in a spherical polar coordinate system and sigma levels in the vertical. A particular feature in this model is the solution of the advective terms based on a Piecewise Parabolic Method (PPM), which handle the solution of sharp gradients in thermoclines and fronts at relatively low numerical diffusion (James, 1996). Details about the model and its validation in the northwest European continental shelf can be found in Holt and James (2001).

The original set of POLCOMS equations was modified in order to include wave–current interactions following the vortex–force formalism (McWilliams et al., 2004; Ardhuin et al., 2008). The numerical model now solves the momentum equation for the quasi–Eulerian velocity, $(\hat{\mathbf{u}}, \hat{w}) = (\mathbf{u}, w) - (\mathbf{U_s}, W_s)$, where $(\mathbf{u}, w)$ are the components of the mean Lagrangian velocity and $(\mathbf{U_s}, W_s)$ are the components of the Stokes drift. In Cartesian (x,y,z) coordinates, the set of governing equations that include wave–current interaction now read,

$$\frac{\partial \hat{\mathbf{u}}}{\partial t} + \hat{\mathbf{u}} \cdot \nabla \hat{\mathbf{u}} + \hat{w} \frac{\partial \hat{\mathbf{u}}}{\partial z} + f \times \hat{\mathbf{u}} + \frac{1}{\rho_w} \nabla p^H - \frac{\partial}{\partial z} \left(K_Z \frac{\partial \hat{\mathbf{u}}}{\partial z} \right) = -f \times \mathbf{U_s} + \mathbf{U_s} \times \omega - \nabla J, \tag{3}$$

$$\frac{\partial \zeta}{\partial t} + \nabla \cdot \mathbf{u} = 0, \tag{4}$$

$$\frac{\partial c}{\partial t} + \nabla \cdot (\mathbf{u} c) + \frac{\partial w c}{\partial z} - \frac{\partial}{\partial z} \left(K_H \frac{\partial \hat{\mathbf{u}}}{\partial z} \right) = 0. \tag{5}$$

In (3), ∇ represents the horizontal differential operator, p^H is the hydrostatic pressure, f the Coriolis parameter, ρ the density, K_Z is the eddy viscosity, ω is the relative vorticity and J is the Bernoulli–head. The accelerations terms associated with wave–current interactions included on the right–hand side of (3) are the Stokes–Coriolis, the vortex–force, and the Bernoulli–head, respectively. In the depth–integrated continuity equation (4), ζ is the sea surface elevation and, in (5), c and K_H are the concentration of a passive tracer and the eddy diffusivity, respectively.

The eddy viscosity and vertical diffusivity parameters are estimated by a κ–ε turbulence closure scheme using a version of GOTM (General Ocean Turbulence Model; Burchard et al., 1999) embedded in POLCOMS. The closure scheme solves an equation for the total kinetic energy ($\hat{k}$) and an equation for the dissipation rate of energy (ε),

$$\frac{\partial \hat{k}}{\partial t} + \frac{\partial}{\partial z} F(\hat{k}) = \hat{P} + B + \varepsilon, \tag{6}$$

$$\frac{\partial \varepsilon}{\partial t} + \frac{\partial}{\partial z} F(\varepsilon) = \frac{\varepsilon}{\hat{k}} \left(c_{\varepsilon 1} \hat{P} + c_{\varepsilon 3} B + c_{\varepsilon 2} \varepsilon \right), \tag{7}$$

where $F(\hat{k})$ and $F(\varepsilon)$ depict the diffusive flux. The production of turbulent kinetic energy includes the buoyancy (B), the currents vertical shear (P), and a parametrization of the Langmuir turbulence in terms of the Stokes drift vertical shear (P_s),

$$\hat{P} = P + P_s, \tag{8}$$

$$P_s = \hat{k}_z \left(\frac{\partial \hat{\mathbf{u}}}{\partial z} + \frac{\partial \mathbf{U_s}}{\partial z} \right). \tag{9}$$

The production of turbulent kinetic energy by Langmuir turbulence is added to the κ–ε following Kantha and Clayson (2004).

The friction velocity, $\mathbf{u}_* = \sqrt{\boldsymbol{\tau}_{atm}/\rho_w}$, which depends on the wind stress $\boldsymbol{\tau}_{atm}$, is used as a boundary condition to compute the momentum flux between the atmosphere and the ocean,

$$K_z \frac{\partial \mathbf{u}}{\partial z} \Big|_{\zeta=0} = \mathbf{u}_*. \tag{10}$$

The wind stress is generally parametrized by a bulk formulation that depends on a drag coefficient C_D, the wind speed vector referred to 10 m above the sea surface, $\mathbf{U}_{10}$, and the air density, ρ_a,

$$\boldsymbol{\tau}_{atm} = \rho_a C_D \mathbf{U}_{10}^2. \tag{11}$$

In the standard version of POLCOMS, a simple parametrization for C_D that depends only on the local wind speed is used (see for instance; Holt and James, 2001).

The WAM (WAve Modelling; Komen et al., 1996) model solves an action balance equation in terms of the wave energy spectrum, $F(\sigma, \theta, x, y, t)$, as a function of the relative frequency, σ, direction, θ, spatial coordinates, (x, y), and time, t. In deep waters, the evolution of the energy spectrum is controlled by three source terms: wind input (S_{in}), non–linear wave–wave interactions (S_{nl}), and white capping dissipation (S_{ds}). The governing equation in the WAM model reads,

$$\frac{\partial F}{\partial t} + \frac{\partial c_x F}{\partial x} + \frac{\partial c_y F}{\partial y} + \sigma \frac{\partial}{\partial \sigma} \left(c_\sigma \frac{F}{\sigma} \right) + \frac{\partial}{\partial \theta} \left(c_\theta F \right) = S_{in} + S_{nl} + S_{ds} \tag{12}$$

where (c_x,c_y) represent the wave propagation velocity in the geographical space, and (c_σ,c_θ) represent the wave energy propagation in frequency–direction space. The wave propagation is affected by the inhomogeneous, unsteady, currents and sea surface elevation fields. The expressions for the wave propagation velocities can be found in Osuna and Monbaliu (2004).

3.6.1 Coupling details

In the coupled version of WAM, the effects of currents on the wave energy propagation are made dependent on the wave frequency, in such a way that the current felt by a specific wave component represents a depth–averaged current according to Kirby and Chen (1989). Information about the three–dimensional Stokes drift, which is used in (3)–(5), and (6)–(7), is computed internally by WAM taking into account the whole spectrum $F(\sigma, \theta, x, y, t)$ according to Mellor (2003, 2005). No assumption about the vertical structure of the Stokes drift is considered.

In the wave–current interaction model system, WAM also computes the necessary information to consider a drag coefficient that depends on the sea state. In this case, the parametrization proposed by Janssen (1991) is used so,

$$C_D = \frac{\kappa^2}{\left[\ln\left(z/z_e\right)\right]^2}, \tag{13}$$

where κ is the von Karman constant and z_e the effective roughness scale. This dependence on the sea state is supported by the effective roughness scale, which is computed as the combination of the roughness length scales associated with gravity–capillary waves (z_0) and gravity waves (z_1).

$$z_e = z_0 + z_1. \tag{14}$$

The roughness length scale, z_0, is calculated through the Charnock relation,

$$z_0 = \alpha u_*^2 / g, \tag{15}$$

where the Charnock parameter (α) is considered constant and equal to 0.144 (Janssen, 2004). Instead, the roughness length scale, z_1, depends on the ratio between the stress felt by the sea surface waves $\boldsymbol{\tau}_w$ and the wind stress $\boldsymbol{\tau}_{atm}$,

$$z_1 = z_0 \left(\frac{1}{\sqrt{1 - |\boldsymbol{\tau}_w|/|\boldsymbol{\tau}_{atm}|}} - 1 \right). \tag{16}$$

To better represent the surface ocean dynamics, Breivik et al. (2015) propose that the stress felt by the currents, $\boldsymbol{\tau}_{oc}$, needs to be computed from a realistic balance of the momentum flux that takes into account the net stress that ends up as ocean waves, $\hat{\boldsymbol{\tau}}_w$, in such a way that,

$$\boldsymbol{\tau}_{oc} = \boldsymbol{\tau}_{atm} - \hat{\boldsymbol{\tau}}_w, \tag{17}$$

with $\boldsymbol{\tau}_{atm}$ computed as in (11), assuming (13)–(16), and $\hat{\boldsymbol{\tau}}_w$ obtained by integrating the wave source terms:

$$\hat{\boldsymbol{\tau}}_w = \rho_w g \int_0^{2\pi} \int_{-\infty}^{\infty} \Big(S_{in} + S_{ds} \Big) c_p^{-1} d\sigma d\theta, \tag{18}$$

where c_p is the phase speed of the wind waves.

The wave–current interaction system, POLCOMS–WAM, allows for the synchronous exchange of information between the wave model and the circulation model (Osuna and Wolf, 2005). WAM is hard–wired to POLCOMS so both models use the same bathymetry and wind data. The exchange of information is carried out on a predefined time step and constrained to be a multiple of the baroclinic time step. Details about the evolution in the development of the coupled version of POLCOMS–WAM, as well as its validation, can be found in Osuna and Wolf (2005), Bolaños et al. (2011), and Bricheno et al. (2013). Although these works have focused more on the impact of wave–current interaction on the sea surface waves at coastal regions, Bolanos et al. (2009) uses the POLCOMS–WAM coupled system to successfully simulate the oceanographic conditions over the Mediterranean Sea. Additionally, comparisons between POLCOMS–WAM and observations carried out in this work show that the coupled system is capable of reproducing the GoT ocean dynamics during Tehuano events.

3.6.2 Models implementation

POLCOMS–WAM implementation for this experiment has a spatial resolution of approximately 3–km. In the WAM model, the directional spectrum is discretized using 24 directions and 32 frequencies, with a logarithmic distribution ranging from 0.037 to 0.716Hz. The coupled system is set to exchange information every 20 min. The bathymetry data used for POLCOMS–WAM comes from GEBCO (General Bathymetric Chart of the Oceans; https://www.gebco.net). The initial and boundary conditions for POLCOMS are taken from HYCOM (HYbrid Coordinate Ocean Model; Bleck, 2002; Chassignet et al., 2003) global $1/12^o$ GLBu0.08 dataset. The boundary conditions for WAM are obtained from a global implementation of WW3 (WaveWatch III®; The WAVEWATCH III ® Development Group (WW3DG), 2016) forced with wind and ice coverage from the CFSR (Climate Forecast System Reanalysis; Saha et al., 2010) dataset.

The atmospheric forcing for the coupled system is taken from a local implementation of the Weather Research and Forecasting (WRF) model for the Gulf of Tehuantepec region. The WRF is the first fully compressible conservative form non-hydrostatic atmospheric model that solves the Euler equations, which was designed for both research and operational applications. It uses a time-split integration scheme in order to deal with meteorological acoustic modes, allowing it to resolve from synoptic scaling processes to meter order processes (Skamarock and Klemp, 2008). The physics package used in this implementation is described in Passalacqua et al. (2016). The model implementation consists of two nested domains. The first domain has a resolution of 12 km, covering the Gulf of Mexico and the Gulf of Tehuantepec. The second domain covers the GoT and has a spatial resolution of 4 km. The initial condition and boundary forcing for WRF are obtained from the CFSR data set.

POLCOMS–WAM is used to reproduce the ocean dynamics in the Gulf of Tehuantepec during the period from September 23 to October 29, 2010.

3.6.3 Total currents decomposition

Stokes drift in POLCOMS–WAM is computed following Bolaños et al. (2011) and the high–frequency contribution has been included according to Breivik et al. (2014). The coupled system implemented in this work explicitly includes the most relevant processes associated with the wave–current interactions for the deep waters case and their effects on the wave spectral evolution.

Total currents simulated by POLCOMS–WAM results from the combination between the quasi–Eulerian current and the Stokes drift ($\mathbf{u} = \hat{\mathbf{u}} + \mathbf{U_s}$) since the model solves the hydrostatic momentum equation by considering into account wave–current interactions. In this way, total currents are conformed by the geostrophic, wind–driven, and remaining ageostrophic currents:

$$\mathbf{u}_{\mathrm{tot}} = \hat{\mathbf{u}}_{\mathrm{geo}} + \mathbf{u}_{\mathrm{wd}} + \mathbf{u}_{\mathrm{rageo}} \tag{19}$$

The geostrophic currents from POLCOMS–WAM are calculated using the geostrophic balance as a function of the ADT (h):

$$f\hat{z}\hat{\mathbf{u}} = -g\nabla h. \tag{20}$$

It is worth noting that in order to eliminate ageostrophic processes in h, which could introduce spurious geostrophic velocities, an inertial period low–pass filter with a latitude dependency is applied.

In order to compute the surface wind–driven currents by POLCOMS–WAM, a balance that includes Ekman currents with a dependence on the Stokes–Coriolis force (Polton et al., 2005; Rascle and Ardhuin, 2009; Song, 2009), a momentum flux balance that depends on the sea state (Janssen, 1991) and inertial oscillations is used:

$$\frac{d\hat{\mathbf{u}}}{dt} + f\hat{z} \times (\hat{\mathbf{u}} + \mathbf{U_s}) = \frac{\partial}{\partial z}\left(K_z \frac{\partial \hat{\mathbf{u}}}{\partial z}\right). \tag{21}$$

The Stokes drift is added to the Ekman currents obtained by POLCOMS–WAM since it is implicitly included in GlobCurrent. In this way, a fairer comparison between the time average of both products during the Tehuano event can be made (Fig. 5).

4 Stokes drift

The mean Stokes drift fields from GlobCurrent and POLCOMS–WAM during the analyzed Tehuano event are shown in Fig. 3. The comparison of these results shows a similar current pattern throughout the domain, with a southward current with a maximum speed of about 0.1 m s^{-1} in GlobCurrent (Fig. 3a) and about 0.2 m s^{-1} in POLCOMS–WAM (Fig. 3b) over the region influenced by the Tehuano event. In terms of magnitude, it is evident that the POLCOMS–WAM model presents higher speeds. This is due to the differences in the wind forcing used in both cases since wave–current interactions do not play

an important role in the modification of the Stokes drift during the Tehuano event (less than 10%). However, several studies have shown that wave–currents interactions can strongly modify sea surface waves in regions with strong western boundary currents, *e.g.,* the Gulf Stream and the Loop Current, Kuroshio Current, and Agulhas Current (Abolfazli et al., 2020; Wang et al., 2020; Allahdadi et al., 2022; de León and Soares, 2022).

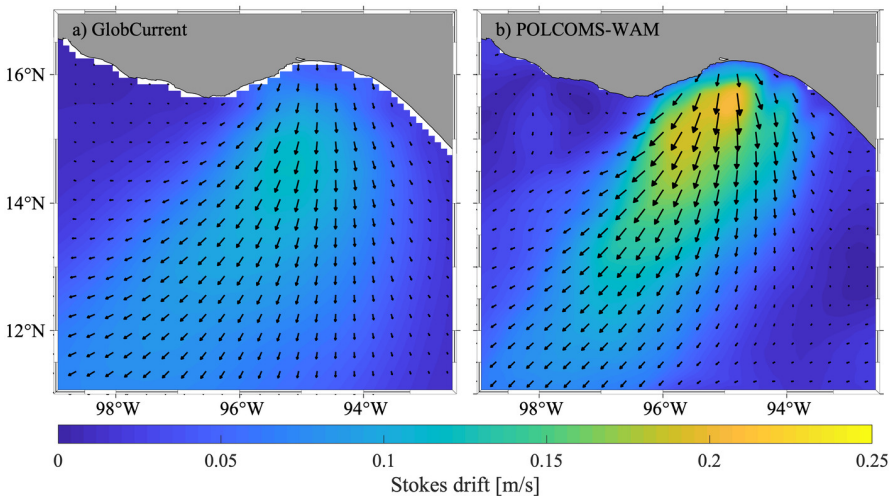

Fig. 3: Surface Stokes drift averaged over the analyzed Tehuano event. GlobCurrent and POLCOMS–WAM estimations are shown in (a) and (b), respectively.

The average wind field obtained from the CFSR dataset and the one computed from WRF dataset during the analyzed Tehuano event are shown in Fig. 4. CFSR data is used as a forcing field to estimate Stokes drift in GlobCurrent (Rascle and Ardhuin, 2013), while WRF model results are used to force POLCOMS–WAM model. CFSR winds exhibit weaker wind speeds in comparison with WRF, especially near the coasts of the GoT, where winds reach speeds up to 18 m s^{-1} in WRF and about 13 m s^{-1} in CFSR. This implies important differences in wind–wave growth and therefore in the calculation of Stokes drift, as observed in Fig. 3. Winds greater than 18 ms^{-1} have been observed near the coast by *in–situ* measurements (approximately 22 km) during the INTOA experiment (Ocampo-Torres et al., 2010), which are underestimated by CFSR by about 40% (not shown). A detailed analysis of the impact of wind underestimation at short fetch on the wave evolution in the Gulf of Tehuantepec area will be presented elsewhere since this topic is beyond the scope of this study.

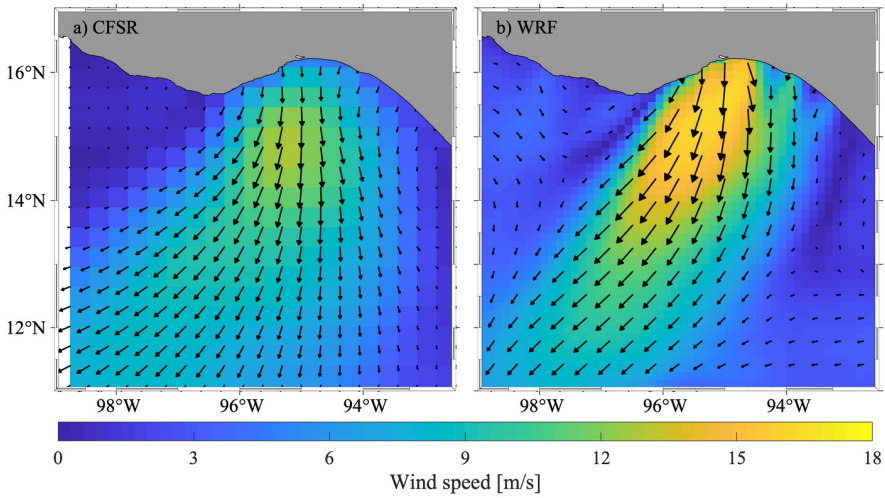

Fig. 4: Wind speed averaged over the analyzed Tehuano event. Results from the CFSR dataset and the WRF model are shown in (a) and (b), respectively.

5 Wind–driven currents

A comparison between the averaged wind–driven currents from GlobCurrent and POLCOMS–WAM is presented in Fig. 5. Spatial patterns of wind–driven currents in both products exhibit broadly the same characteristics, with the largest speeds (about 0.8 m s^{-1}) between 12°N and 16°N. It is worth mentioning that, according to Polton (2015), including Stokes drift in the Ekman balance results in a better estimate of the direction of wind-driven currents. In the POLCOMS–WAM implementation, the inclusion of $\mathbf{U_s}$ in the estimate of wind–driven currents induce differences of about 15° (not shown). However, it is observed that the spatial distribution of wind–driven currents from GlobCurrent is more homogeneous than the computed by POLCOMS–WAM, since the numerical implementation is able to solve small–scale processes due to its higher spatial resolution (∼3 km). In addition, wind-driven currents calculated by POLCOMS-WAM over the Upper Gulf of Tehuantepec (between 0.50 and 0.65 m/s) are less intense than those estimated by GlobCurrent (0.8 m/s). A numerical analysis of wave–currents interaction over the sea surface layer during a Tehuano event that occurred in March 2005 (not included here) shows that sea surface current speeds in the upper Gulf of Tehuantepec tend to decrease by about 15%. This decrease in the sea surface speed is related to two processes: on the one hand, a deflection on the Ekman profile due to the Stokes–Coriolis force, while on the other hand, part of the wind stress is used to generate wind waves in the coupled model (see equation 17). Moreover, numerical results show the presence of wind–driven currents with strong speeds surrounding the

anticyclonic eddy. This result could be related to the fact that in POLCOMS–WAM the wind stress vertical diffusion depends on the vertical shear of the quasi–Eulerian currents (right side of equation 21), whereas in the Ekman theory formulation it is assumed that the vertical shear of currents is generated principally by the wind. As a consequence, the Ekman currents computed by POLCOMS–WAM could be contaminated by vertical shear associated with non–Ekman currents.

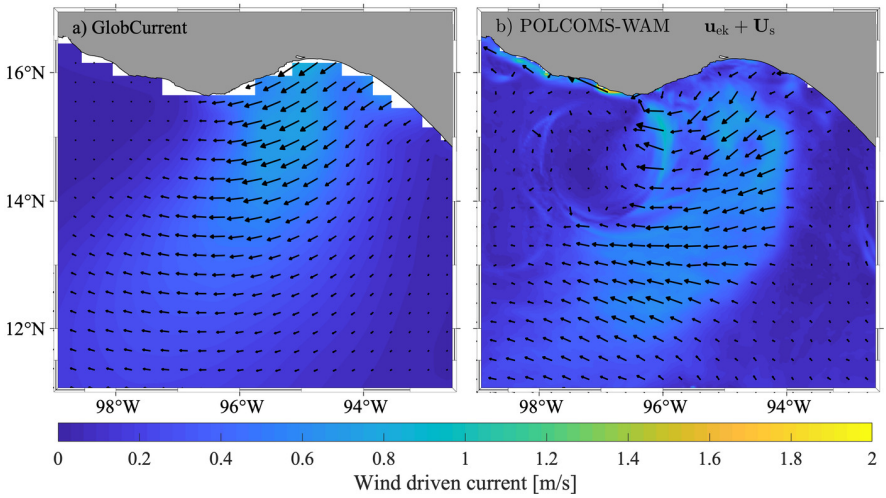

Fig. 5: Mean wind–driven currents averaged over the analyzed Tehuano event. Current vectors at the sea surface corresponding to GlobCurrent and POLCOMS–WAM are shown in (a) and (b), respectively.

6 Geostrophic currents

The averaged geostrophic current field during the Tehuano event from GlobCurrent (Fig. 6a) shows a poleward current at ∼94°W of about 0.4 m s^{-1} which gives rise to a coastal current in the GoT (∼0.45 m s^{-1}), and the presence of a large anticyclonic eddy west of the GoT. The cyclonic eddy displays weaker currents (∼0.9 m s^{-1}) and an irregular shape, whereas in POLCOMS–WAM the eddy shows current speeds of about 1.4 m s^{-1} and a more symmetrical shape (Fig. 6b).

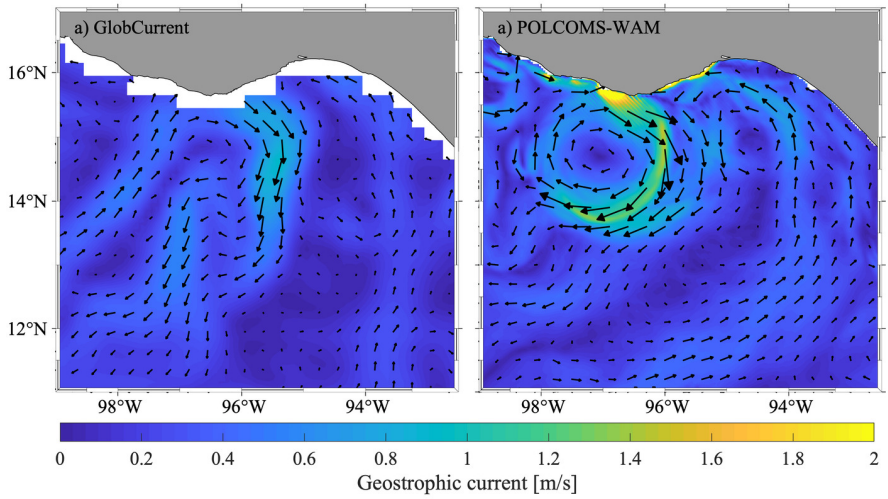

Fig. 6: Surface geostrophic currents averaged over the analyzed Tehuano event period. Results of GlobCurrent and POLCOMS–WAM are shown in (a) and (b), respectively.

It is possible that the anticyclonic eddy velocities reproduced by POLCOMS–WAM could be related to model biases. However, these differences could also be associated with the lack of spatial and temporal resolution in altimetric along–track arrays used to produce gridded products such as MDT or SLA (Chelton et al., 2011; Amores et al., 2018; Archer et al., 2020). In order to assess this, an approximation of the GlobCurrent ADT anomalies, $h' = h - \bar{h}$, where $\bar{h}$ correspond to the spatial average of h, are computed as the sum of the CMEMS sea level anomaly and the MDT products CNES–CLS13 and CNES–CLS18 (Fig. 7). In both cases, ADT anomalies exhibit values between -0.16 and 0.28 m, indicating that CNES–CLS18 MDT does not seem to play an important role in modulating the shape and intensity of the anticyclonic eddy. However, currents east of the negative ADT anomaly tongue exhibit relevant improvements. Here, the poleward current at ∼94°W is better defined when using the CNES–CLS18 MDT but also the coastal current east of the GoT. POLCOMS–WAM results (Fig. 7c) are in better agreement with the results obtained from CNES–CLS18.

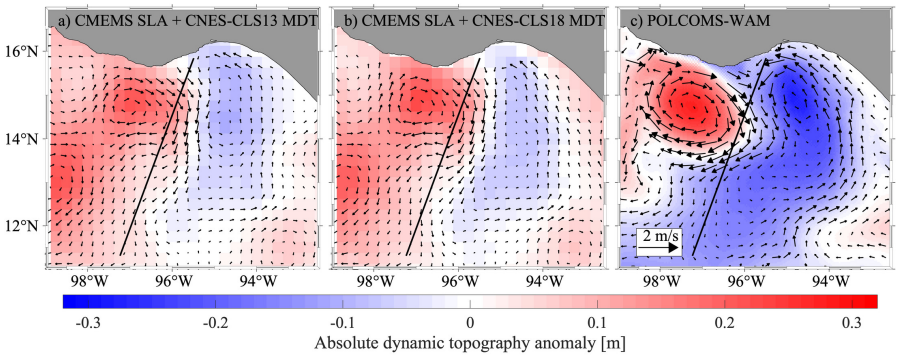

Fig. 7: Absolute dynamic topography anomaly corresponding to October 20, 2010. a) CMEMS as SLA plus CNES–CLS13. b) CMEMS as SLA plus CNES–CLS18. c) POLCOMS–WAM. All figures include the CTOH along–track trajectory corresponding to that date (diagonal stripe).

Filtered SLA estimations from an altimeter along–track from CTOH are used as a reference to assess the differences in the ADT anomalies and the geostrophic current speed between POLCOMS–WAM and GlobCurrent on January 20, 2010. In order to compare with CTOH, sea level anomalies from CMEMS are used to mimic GlobCurrent. The altimeter track is depicted in Fig. 7, where can be observed that it crosses along the edge of the anticyclonic eddy computed by POLCOMS–WAM since the eddy is shifted northward in comparison with the anticyclonic eddy observed by GlobCurrent and CMEMS. In spite of this, the along–track ADT (sea level anomaly plus CNES–CLS13 and CNES–CLS18 MDT) anomalies from CTOH and POLCOMS–WAM show equivalent slopes across the eddy in comparison with the relatively weaker CMEMS ADT anomalies (Fig. 8a).

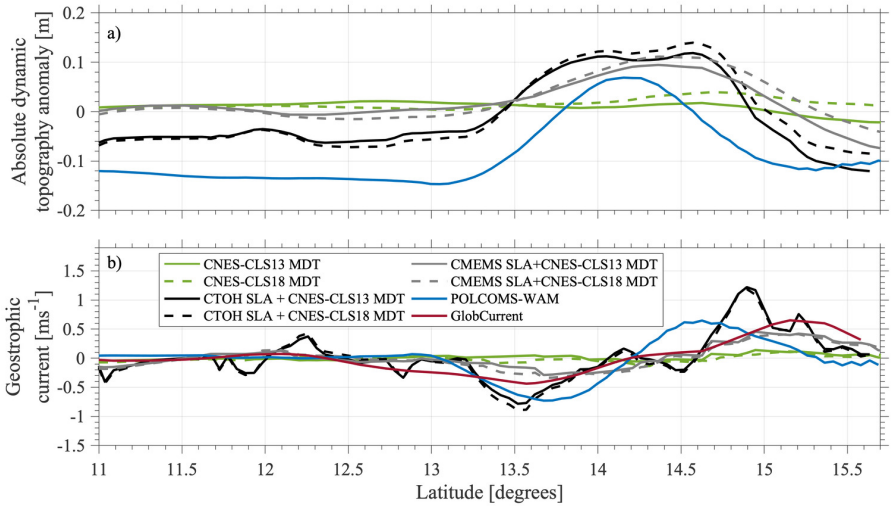

Fig. 8: Along–track absolute dynamic topography anomaly (a) and its corresponding geostrophic currents component (b).

The component of the geostrophic current speed perpendicular to the satellite track is then compared with the corresponding geostrophic currents of the GlobCurrent, CMEMS, and POLCOMS–WAM (see Fig. 8b). It can be observed that in the southern eddy edge, the CTOH geostrophic speeds are of the same order as the computed by POLCOMS–WAM ($\sim$0.8 m s^{-1}). Besides, the CTOH product shows velocities up to 1.2 m s^{-1} in the northern eddy edge, showing that the geostrophic currents related to the anticyclonic eddy in CMEMS and GlobCurrent are underestimated. In addition, as previously mentioned, it can be observed that computing the ADT anomalies with the CNES–CLS18 MDT does not show significant differences in the intensity of the anticyclonic eddy geostrophic currents.

As suggested by Trasviña and Barton (2008), the underestimation of the geostrophic current speed could be related to limitations in the spatial and temporal resolution of the satellite tracks, the smoothness that results from merging the altimeters data into a regular grid, and the variability that the Tehuano winds induce on mesoscale eddies. The asymmetrical shape of the anticyclonic eddy in GlobCurrent could be also associated with the lack of spatial resolution in SLA gridded products resulting from the combination of the satellite along–track data. This has been demonstrated for geostrophic eddies in the North Atlantic Ocean and the Mediterranean Sea by Amores et al. (2018). Through a reconstruction of synthetic SLA maps from realistic numerical simulations, the authors have shown that gridded products resulting from the merging of along–track altimetry data are potentially unable to characterize the mesoscale variability. Additionally, the authors found that artificially larger eddies can be produced from the lack of spatial resolution in

combined satellite along–track data, promoting that clusters of small eddies be aliased as larger ones.

In this context, an analysis of the variability that corresponds to 7 days (from October 12 to October 18, 2010) of the GlobCurrent geostrophic currents under the influence of the Tehuano event is shown in Figure 9. The analysis reveals that the GlobCurrent product presents similar current patterns throughout the 7 days (Figure 9a-c), with a higher standard deviation of about 0.2 m s^{-1} (Figure 9d).

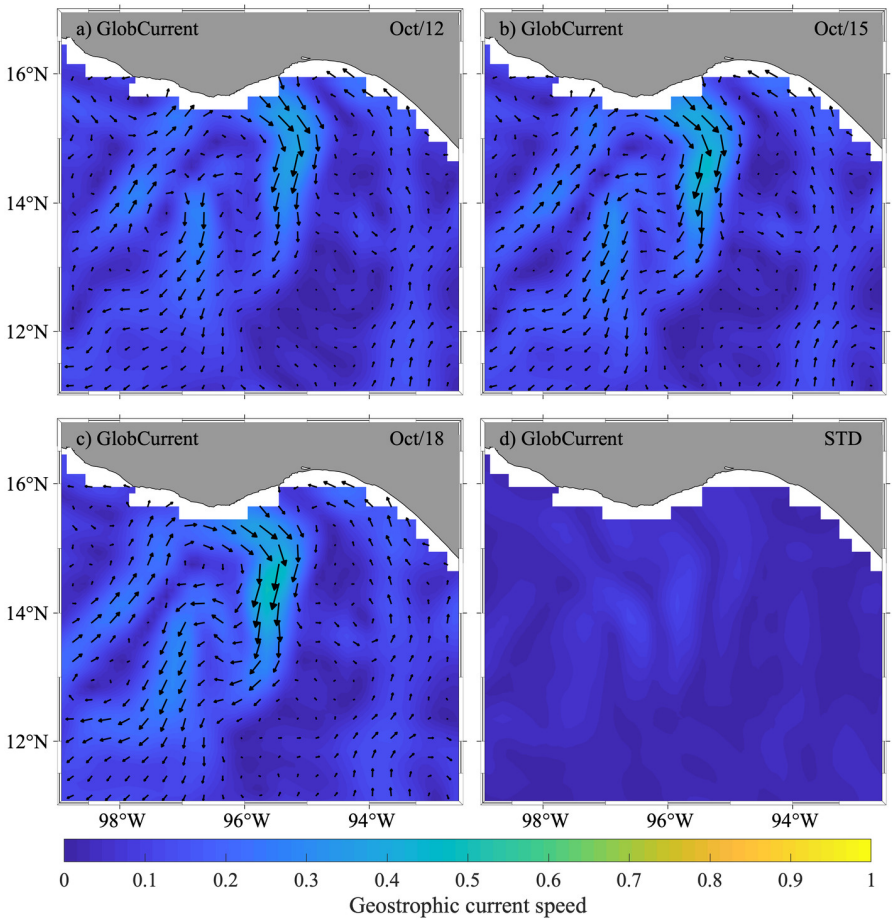

Fig. 9: Evolution of the GlobCurrent geostrophic current speed from October 12 to October 18, 2010 (a–c), as well as their corresponding standard deviation (d).

In contrast, the variability analysis in POLCOMS–WAM (Figure 10) shows that the anticyclonic eddy travels westward and exhibits a larger time–space

variability. This presents an elongated (∼0.72 of eccentricity) shape with higher speeds (about 1.1 m s^{-1}) in its southeastern region (Figure 10a). Afterward, the eddy exhibits a symmetrical shape (∼0.86 of eccentricity) with higher speeds (around 1.5 m s^{-1}) in its eastern region (Figure 10b). Finally, the eddy becomes asymmetrical (∼0.76 of eccentricity) and shows higher velocities (about 1.5 m s^{-1}) in its southeastern region (Figure 10c). Additionally, the presence and evolution of small geostrophic structures can be observed around the anticyclonic eddy (Figures 10a–c). The corresponding standard deviation for the 7 days period of the POLCOMS–WAM geostrophic currents shows high variability (about 0.6 m s^{-1}) in the anticyclonic eddy periphery, as well as in the southwest of the eddy (Figure 10d).

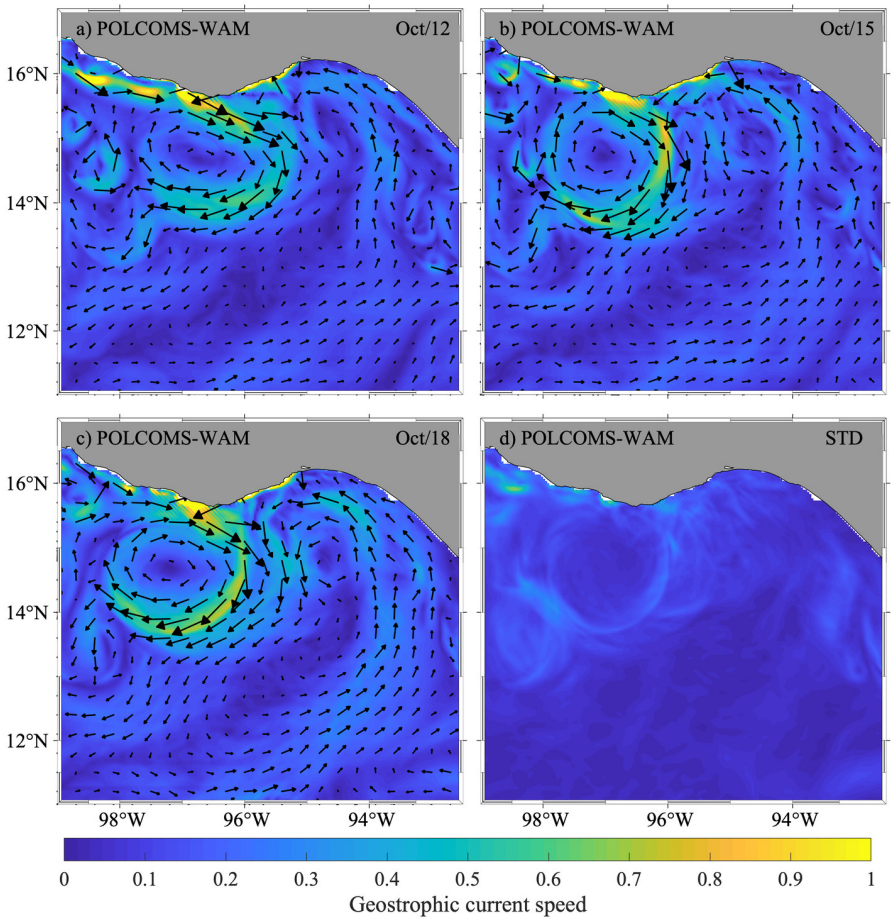

Fig. 10: Evolution of the POLCOMS–WAM geostrophic current speed from October 12 to October 18, 2010 (a–c), as well as the corresponding standard deviation (d).

By comparing both GlobCurrent and POLCOMS–WAM results, it can be inferred that the lack of spatial resolution in combined along–track satellite data can produce larger eddies since small geostrophic structures can be aliased as large mesoscale eddies (Amores et al., 2018). It is possible that a better geostrophic current speed estimation could be obtained when the higher–resolution altimetry mission SWOT (Surface Water and Ocean Topography) be in operation, which will provide sea surface height observations down to 15–30 km in wavelength (Morrow et al., 2019).

7 Total and cyclogeostrophic currents

In order to assess the viability of reconstructing total currents as a combination of geostrophic and wind–driven currents, a comparison between the reconstructed total currents from GlobCurrent and POLCOMS–WAM is shown in Fig. 11a and Fig. 11b, respectively. The mean surface currents of both products show the following pattern: a northward geostrophic current around 94°W, which is affected by the wind–driven currents next to the coastline, becoming a strong westward current (about 1 m s^{-1} in GlobCurrent and 1.2 m s^{-1} in POLCOMS–WAM). This current converges with a geostrophic current generated by an anticyclonic eddy and produces a southwestward current that is intensified by the wind–driven currents (about 1.4 m s^{-1} in GlobCurrent and 1.7 m s^{-1} in POLCOMS–WAM). When this current pattern is compared with the total currents from POLCOMS–WAM (Fig. 11c), it is possible to observe the presence of intense currents ($\sim$1.6 ms^{-1}) in the anticyclonic eddy that represent about 65% of the magnitude of the total currents (Fig. 11d).

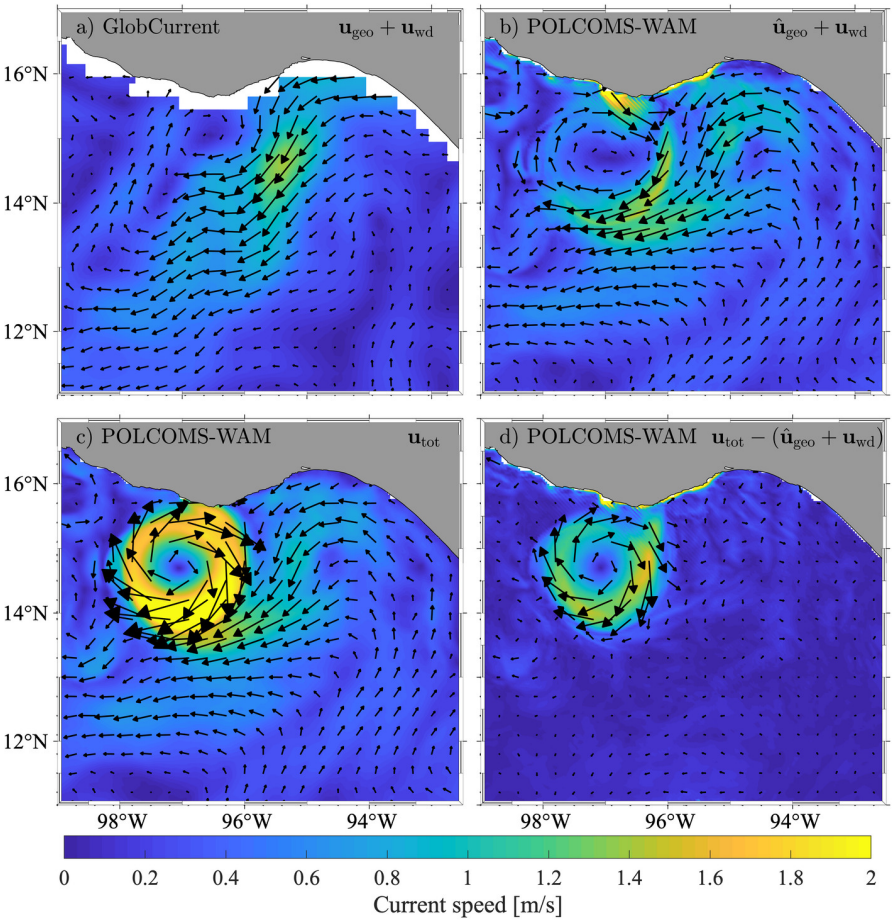

Fig. 11: Ocean currents averaged over the analyzed Tehuano event. The top panels show the values computed at the sea surface by GlobCurrent (a) and POLCOMS–WAM (b), using a linear combination of geostrophic and wind–driven currents. Bottom panels indicate the values of the total currents (c) and the residual ageostrophic (once wind–driven currents are subtracted) currents computed by POLCOMS–WAM (d).

There is no doubt that a part of the overestimation in the eddy velocities is related to model biases. However, although mesoscale eddies are considered in geostrophic balance, there are eddies with strong rotational speed where the advection, and in particular the centrifugal force, have the same order of magnitude as the pressure gradient and the Coriolis force. This condition is known as the gradient wind or cyclogeostrophic balance (Douglass and Richman, 2015; Penven et al., 2014):

$$\hat{\mathbf{u}} \cdot \nabla \hat{\mathbf{u}} + f\hat{z} \times \hat{\mathbf{u}} = -g\nabla\eta. \tag{22}$$

By comparing the dominant terms in the momentum equation (Fig. 12), it is readily apparent that the anticyclonic eddy is in cyclogeostrophic balance. The acceleration of the centrifugal force is of the same order as the acceleration of the Coriolis force (Fig. 12c and 12b, respectively) and in this particular case, the centrifugal force acceleration shows a higher magnitude than the acceleration of the pressure gradient force (Fig. 12a).

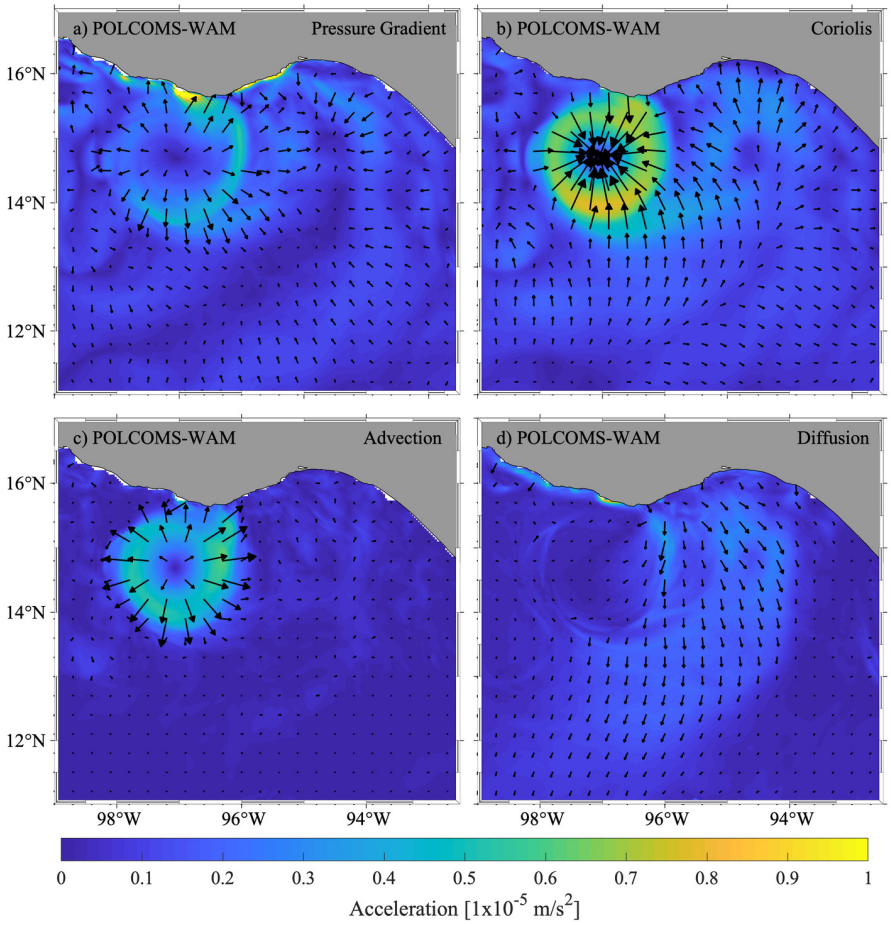

Fig. 12: Average of the main acceleration terms in the momentum equation calculated by POLCOMS–WAM over the Tehuano event. The panels show the accelerations corresponding to the pressure gradient (a), Coriolis (b), centrifugal (c), and diffusion (d).

How the gap–winds induce a cyclogeostrophic balance in the anticyclonic eddies of the Gulf of Tehuantepec can be explained by the relative vorticity of surface geostrophic currents ($\nabla \times \hat{\mathbf{u}}_{geo}$) and the Ekman pumping ($\frac{1}{\rho_w f}\nabla \times \boldsymbol{\tau}$) produced by the Tehuano event (Fig. 13). Since the anticyclonic eddy has a relative vorticity of about $-3{\times}10^{-5}$ s^{-1} (Fig. 13a) and due to the fact that the Tehuano event produces an additional pumping of about -30 m/day over the anticyclonic eddy (Fig. 13b), it is proposed that the Ekman pumping (with the same sign that the relative vorticity of the anticyclonic eddy) could induce a cyclogeostrophic balance by increasing the rotation speed and centrifugal acceleration of the eddy. This is in agreement with other studies (Amedo-Repollo et al., 2019; Azevedo Correia de Souza et al., 2015) that have demonstrated, through a vorticity balance, that the wind stress curl generated by the interaction between wind jets and mountainous islands plays an important role in the generation and evolution of eddies.

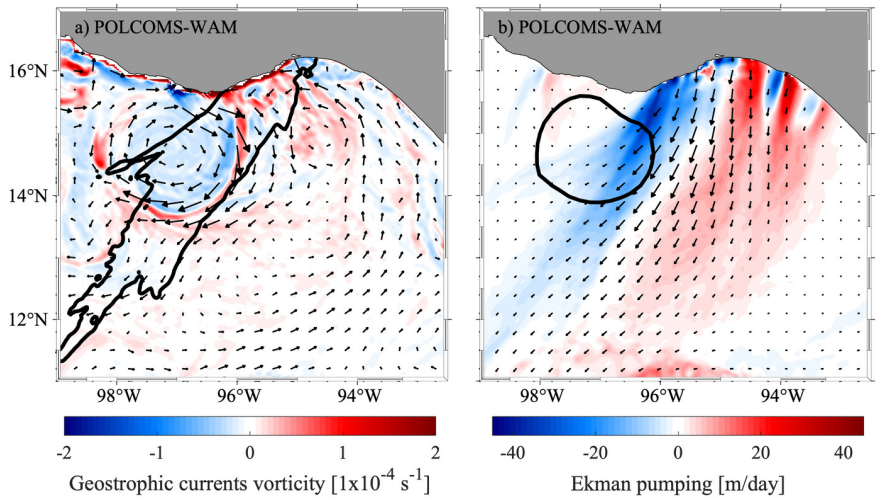

Fig. 13: Relative vorticity of surface geostrophic currents (a) and Ekman pumping (b) averaged over the analyzed Tehuano event. The negative Ekman pumping acting on the anticyclonic eddy is represented by the black contour in figure (a). The position of the anticyclonic eddy is delimited by the black contour in figure (b).

Notwithstanding, it is possible that this implementation of POLCOMS–WAM could generate an overestimation in the wind stress since prescribed atmospheric forcings are used as surface boundary conditions. Our model thus omits any feedback mechanisms between the ocean and the atmosphere. Renault et al. (2016, 2017) have demonstrated that the current feedback dampens the ocean mesoscale activity when a spatially homogeneous wind blows over an eddy, inducing a surface stress curl opposite to the eddy vorticity and a wind

adjustment that counteract the surface stress reduction. These modifications in the stress and wind curl are the result of a drag force that surface currents exert over the atmosphere. This process leads to a decrease (increase) of the wind stress and an increase (decrease) of the wind speed in the presence of surface currents with the same (opposite) wind direction. Considering that over the anticyclonic eddy the wind is not spatially homogeneous, with intense speeds at the east decreasing to the west of the eddy, it can be suggested that the curl of the gap–wind stress could produce a cyclogeostrophic balance by inducing an Ekman pumping in the anticyclonic eddies, even if current feedback mechanisms are considered. Nevertheless, full atmosphere–ocean coupled simulations and field experiments are needed to quantify the current feedback and their effect on the attenuation rate of the anticyclonic eddies in the Gulf of Tehuantepec.

7.1 Evidence of cyclogeostrophic eddies in the Gulf of Tehuantepec

In order to show evidence of a cyclogeostrophic balance in mesoscale eddies of the Gulf of Tehuantepec, data from two drift buoys used by Trasviña and Barton (2008) to characterize the Costa Rica Coastal Current are used in this study. The surface drifters were released in July 2000, a season of the year during which gap–winds are commonly generated by a pressure gradient between a low–pressure system in the Gulf of Tehuantepec and the westward displacement and intensification of the Bermuda high–pressure system (Romero-Centeno et al., 2003).

Figure 14a shows a time series of the wind speed (thin black line) computed by CFSR in the location marked with a red triangle in Fig. 14b,c. Over the month of July, 4 gap–wind events were detected (areas with gray colors in Figs. 14a) that lasted between 3 to 5 days and reached speeds between 4 and 14 m s^{-1}. In order to identify these events, the low–frequency wind speed (wind speed with a period longer than one day; black thick line in Fig. 14a) larger than 7 m s^{-1} (segmented black line in Fig. 14a) was used as a criterion.

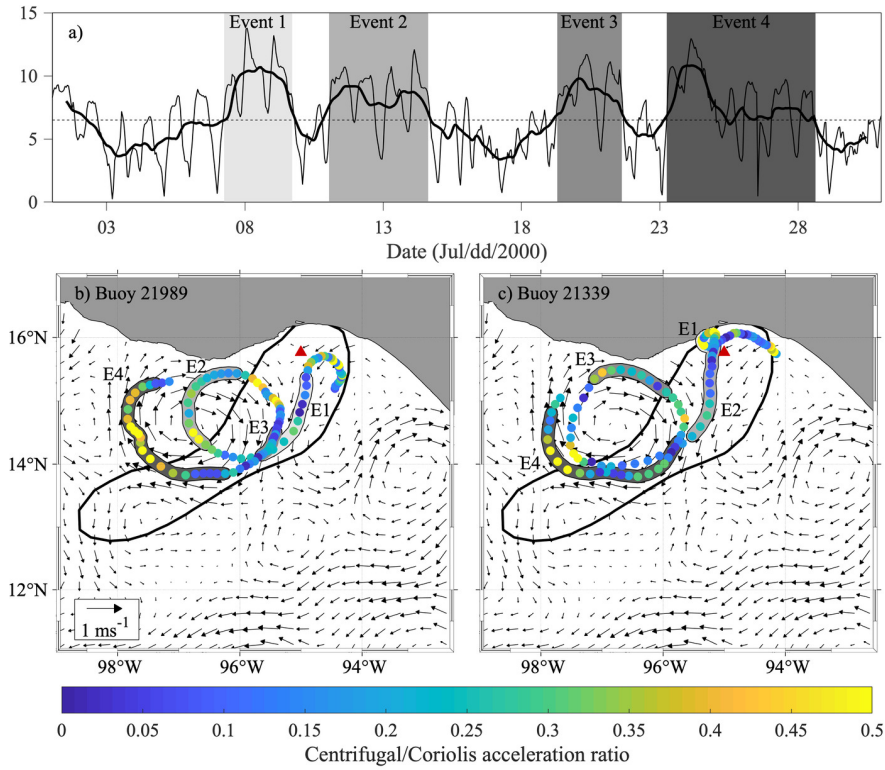

Fig. 14: Time series of the CFSR wind magnitude (thin black line) over July 2000 that correspond to the location marked with the red triangle in the lower panels. The thick line in the upper panel shows the low–frequency variability of the wind magnitude obtained by applying an inertial period low–pass filter. The gray colored areas are included to identify four gap–wind events (top and lower panels). The lowers panels represent the trajectories of buoys 21989 (b) and 21339 (c). The ratio between centrifugal and Coriolis accelerations are also included (colored dots), as well as the time–averaged CMEMS geostrophic currents (black arrows) and 5.5 m s^{-1} wind speed isotach during the last gap–wind event.

Buoys trajectories and the ratio between centrifugal and Coriolis accelerations of the buoys are shown in Figures 14b,c and 14c, together with the periods during which the gap–wind events occurred. The centrifugal acceleration is computed as $\hat{u}_\theta / R$, where $\hat{u}_\theta$ is the tangential velocity and R is the radius of curvature. Also, both figures include the time–averaged geostrophic currents from CMEMS (black arrows) during the last gap–wind event, as well as the 5.5 m s^{-1} wind speed isotach from CFSR to delimitate the region that is influenced by the last event. It is possible to observe that the buoys have higher centrifugal accelerations when gap–wind events occur, accounting for

up to 50% of the acceleration due to Coriolis force. The first gap–wind event carries the buoys towards the anticyclonic eddy located at the west of the Gulf of Tehuantepec. Then, during the last gap–wind event the buoys in the anticyclonic eddy increase their centrifugal acceleration even in the regions that are not forced by the gap–winds (west and northwest of the anticyclonic eddy), suggesting that the gap–wind events enhance the rotation speed of the eddies. These results show that anticyclonic eddies in the Gulf of Tehuantepec can exhibit cyclogeostrophic balance when forced by gap–winds.

7.2 Improvement on the reconstructed currents

Several studies (Penven et al., 2014; Douglass and Richman, 2015) have demonstrated the importance of including a cyclogeostrophic correction in currents that are estimated from altimetry measurements of sea surface height. In order to find a method that presents the most accurate cyclogeostrophic correction, Penven et al. (2014) compare three different methods to better reproduce the surface currents in the Mozambique Channel. The authors find that the iterative method proposed by Arnason et al. (1962) and Endlich (1961), although computationally expensive, produces better correction of surface currents by reducing errors from 0.5 m s^{-1} to 0.1 m s^{-1} (relative errors from 50% to 5%). The iterative method,

$$\mathbf{u}^{n+1} = \mathbf{u}_{\text{geo}} + \frac{\hat{k}}{f} \times (\mathbf{u}^n \cdot \nabla \mathbf{u}^n)\,, \tag{23}$$

uses the geostrophic currents ($\mathbf{u}_{\text{geo}}$) as initial condition. Penven et al. (2014) propose an iterative method where the solution of (23) is found using point–by–point iterations until the residual $|\mathbf{u}^{n+1} - \mathbf{u}^n|$ becomes smaller than 0.01 m s^{-1} or starts to increase.

The cyclogeostrophic balance is computed from the GlobCurrent and POLCOMS–WAM geostrophic currents following the methodology of Penven et al. (2014). In the GlobCurrent, the cyclogeostrophic correction generates an increase of between 20% and 35% (0.4 m s^{-1} and 0.65 m s^{-1}, respectively) in the reconstructed current ($\mathbf{u}_{\text{totrcyc}} = \mathbf{u}_{\text{cyc}} + \mathbf{u}_{\text{wd}}$) speed west and southwest of the anticyclonic eddy (Fig. 15). As in GlobCurrent, POLCOMS–WAM also exhibits reconstructed currents between 20% and 35% stronger when including the cyclogeostrophic correction, reaching current speeds above 1.8 m s^{-1} in the southeastern edge region of the anticyclonic eddy, and speeds above 0.8 m s^{-1} in its northwestern edge region (Fig. 16b). In order to quantify the error resulting from the reconstruction of the POLCOMS–WAM total currents by including or excluding a cyclogeostrophic correction, a comparison between the total currents ($\mathbf{u}_{\text{tot}}$) and the reconstructed currents with ($\mathbf{u}_{\text{totrcyc}} = \hat{\mathbf{u}}_{\text{cyc}} + \mathbf{u}_{\text{wd}}$) and without ($\mathbf{u}_{\text{totr}} = \hat{\mathbf{u}}_{\text{geo}} + \mathbf{u}_{\text{wd}}$) the cyclogeostrophic correction has been carried out. Comparing the total currents with the reconstructed currents without the correction (Fig. 16c), it is evident that the reconstructed currents underestimate the velocities by up to 1.6 m s^{-1} (between 65% and 80% of the current velocity) in the east and southwest regions of the eddy between its center and

its edge. On the other hand, a comparison between the total currents and the reconstructed currents that include the cyclogeostrophic correction (Fig. 16c) shows that the reconstructed currents underestimate speeds by up to 1.4 m s^{-1} (between the 55% and 70% of the current speed) in the same region.

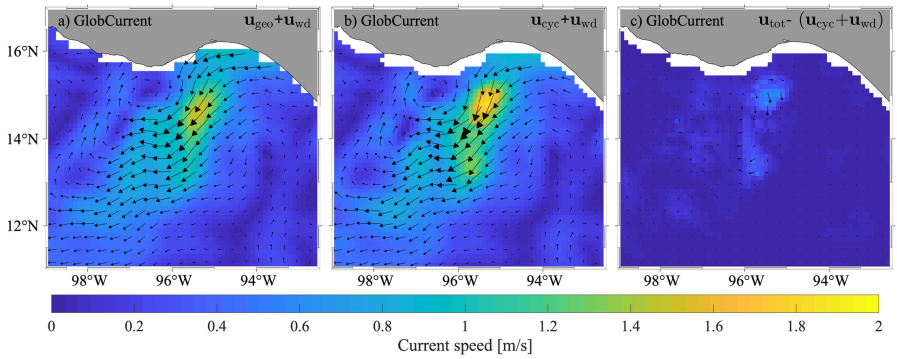

Fig. 15: Time–averaged of the GlobCurrent reconstructed ocean currents with (b) and without (a) the cyclogeostrophic correction, in addition to a comparison between the products (c).

In spite of the decrease of the error when reconstructing the total currents considering the cyclogeostrophic correction, Penven et al. (2014) obtain better results when implementing the iterative method in the mesoscale eddies found in the Mozambique Channel Ring. In their work, Penven et al. (2014) apply the iterative method in high energetic eddies that reached current speeds of 2 m s^{-1}, but with small centrifugal accelerations, attaining only up to a third of the pressure gradient accelerations (Fig. 17a). For the case of the anticyclonic eddy in the Gulf of Tehuantepec, the centrifugal acceleration is up to three times larger than the pressure gradient acceleration (Fig. 17b) as a result of the Ekman pumping that is generated by the Tehuano event.

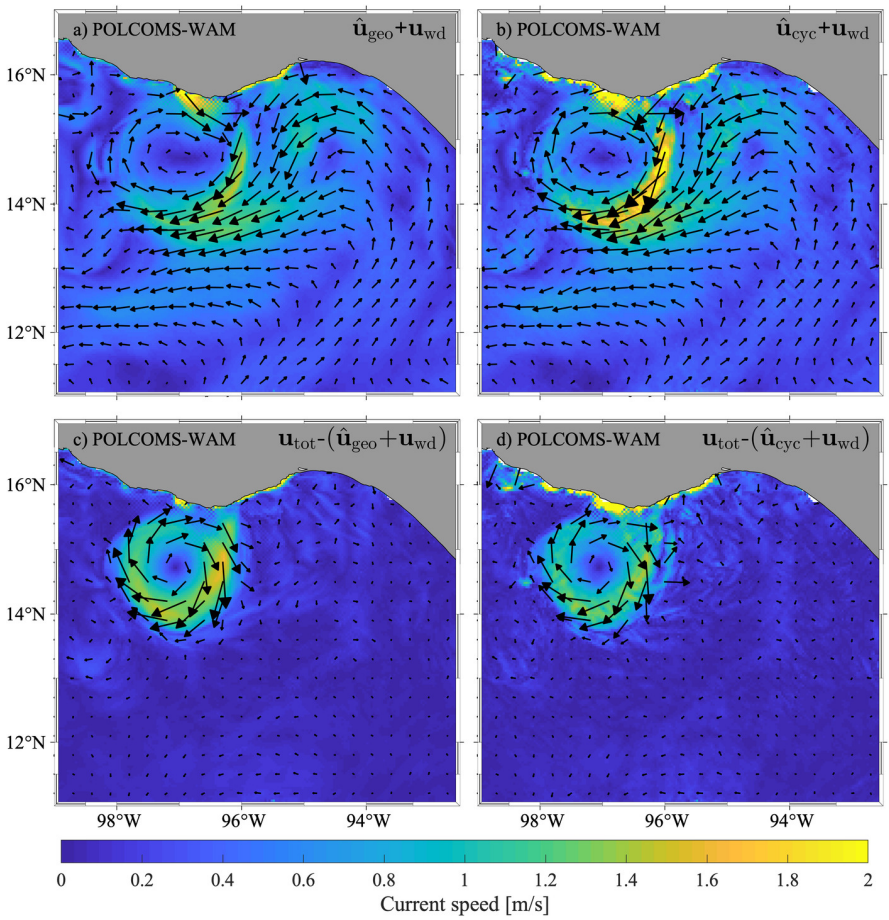

Fig. 16: Time–averaged of the POLCOMS–WAM reconstructed ocean currents with (b) and without (a) the cyclogeostrophic correction, as well as a comparison with the total currents (d and c, respectively).

Taking into account these differences in the eddies properties, a cyclogeostrophic correction can be applied to improve geostrophic currents derived from altimeter products, as proposed by Penven et al. (2014). Nevertheless, special care should be taken in regions with strong winds events, such as the Gulf of Tehuantepec, where Tehuano winds can strongly force mesoscale eddies, leading to a cyclogeostrophic balance dominated by the centrifugal force.

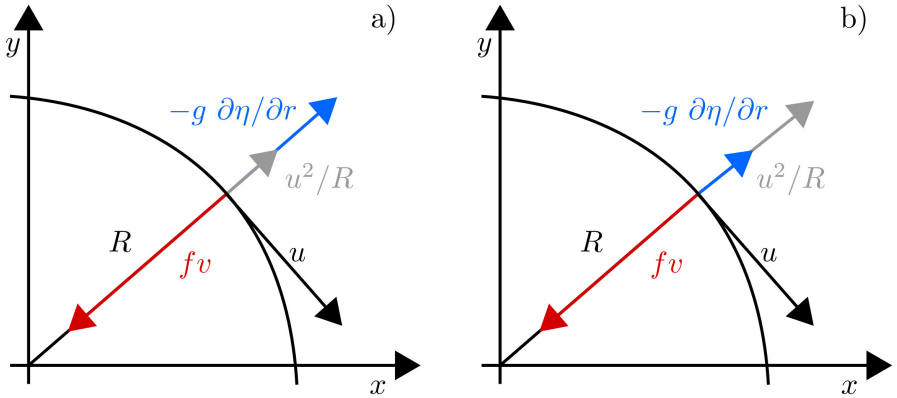

Fig. 17: Diagrams of the forces that interact in a wind gradient balance for an anticyclonic eddy in the northern hemisphere (modified from Penven et al., 2014). a) Regular case. b) Anticyclonic eddy under the influence of strong gap–wind conditions.

8 Summary and conclusions

This work analyzed the ability of GlobCurrent to reproduce the mesoscale dynamics response during a gap–wind event in the Gulf of Tehuantepec, Mexico between October 13 and October 19, 2010. To achieve this, the GlobCurrent dataset is compared with altimetric and buoy observations, but also with a high–resolution numerical results from the POLCOMS–WAM coupled system.

The numerical model results show that the estimation of Stokes drift in the study area strongly depends on the wind field, especially in the near-shore region. An underestimation of the wind speed, especially at short fetch, leads to an underestimation of the wave field offshore, and therefore an underestimation of the Stokes drift. Wind–driven current fields from GlobCurrent are well reproduced by POLCOMS–WAM when considering the Stokes Drift in the Ekman balance, indicating that wave–current interactions are important to better reproduce wind–driven currents.

T here is a good agreement in the main circulations patterns in GlobCurrent and POLCOMS–WAM, which consist of a poleward current around -94°W that turns into a northwestward coastal current east of the GoT. Besides, both GlobCurrent and POLCOMS–WAM exhibit the presence of a large anticyclonic eddy west of the GoT. Nevertheless, some differences between GlobCurrent and the numerical results related to the magnitude and shape of an anticyclonic eddy west of the study area are found. POLCOMS–WAM results reproduce a more vigorous and more symmetrical eddy than the one reported by GlobCurrent. Differences might be associated with the limited spatial and temporal resolution of the satellite array measurements that GlobCurrent

uses to compute geostrophic currents, in particular, to determine the shape and intensity of the entire eddy. Future high–resolution measurements of sea surface height from the SWOT altimetry mission could improve the geostrophic product of GlobCurrent.

According to the total current fields calculated by GlobCurrent and the numerical model results, it is found that most of the circulation patterns in the Gulf of Tehuantepec during the Tehuano event can be obtained from the linear sum of the geostrophic current fields and the Ekman currents. The total current estimation of GlobCurrent could be improved by including a cyclogeostrophic correction of altimetry gridded products through the iterative method proposed by Arnason et al. (1962) and Endlich (1961), and tested by Penven et al. (2014). However, cyclogeostrophic currents related to wind–forced mesoscale eddies, together with other transient ageostrophic contributions (like near-inertial motions; Ubelmann et al., 2021) are important limitations to be overcome in the development of more accurate surface current products, as for instance attempted within the ESA World Ocean Circulation (WOC) project. Finally, the ocean response to gap–winds should be studied in other regions of the world, for example, the Gulf of Genoa, the Hawaiian Islands, and the lee of the Philippines region at the South China Sea.

Acknowledgments. This is a contribution of CONACYT–FOINS project 219582 through Mexico-Belgium bilateral co–operation. Special thanks to L.A. Julieta Castro for her support in logistics and administrative procedures throughout the project. Special thanks to Fernando Niño and Fabien Blarel for their help in providing the CTOH data. Support from Basic Science–CONACYT projects 155793, 168173, and 255377 are also acknowledged. Aimie Moulin was funded by the Mexican National Council for Science and Technology - Mexican Ministry of Energy - Hydrocarbon Fund, project 201441 (CIGoM).

Declarations

- Funding: This is a contribution of CONACYT–FOINS project 219582 through Mexico–Belgium bilateral co-operation. Support from Basic Science–CONACYT projects 155793, 168173, and 255377. Aimie Moulin was funded by the Mexican National Council for Science and Technology - Mexican Ministry of Energy - Hydrocarbon Fund, project 201441 (CIGoM).
- Conflict of interest/Competing interests (check journal-specific guidelines for which heading to use): Not applicable
- Ethics approval: Not applicable
- Consent to participate: All the authors agree with the full content of the document and the authorship order.
- Consent for publication: All the authors agree with the full content of the document and its publication.
- Availability of data and materials: Not applicable
- Code availability: Not applicable
- Authors' contributions: All authors contributed equally to this work.

References

Abolfazli, E., J.H. Liang, Y. Fan, Q.J. Chen, N.D. Walker, and J. Liu. 2020, July. Surface gravity waves and their role in ocean-atmosphere coupling in the gulf of mexico. *Journal of Geophysical Research: Oceans 125*(7). https://doi.org/10.1029/2018jc014820 .

Allahdadi, M.N., R. He, and V.S. Neary. 2022, December. Impact of the gulf stream on ocean waves. *Deep Sea Research Part II: Topical Studies in Oceanography*: 105239. https://doi.org/10.1016/j.dsr2.2022.105239 .

Amador, J.A., E.J. Alfaro, O.G. Lizano, and V.O. Magaña. 2006. Atmospheric forcing of the eastern tropical pacific: A review. *Progress in Oceanography 69*(2-4): 101–142 .

Amedo-Repollo, C.L., X. Flores-Vidal, C. Chavanne, C.L. Villanoy, and P. Flament. 2019. Low-frequency surface currents and generation of an island lee eddy in panay island, philippines. *Journal of Physical Oceanography 49*(3): 765–787. https://doi.org/10.1175/JPO-D-17-0191.1 .

Amores, A., G. Jordà, T. Arsouze, and J. Le Sommer. 2018. Up to what extent can we characterize ocean eddies using present-day gridded altimetric products? *Journal of Geophysical Research: Oceans 123*(10): 7220–7236 .

Archer, M.R., Z. Li, and L.L. Fu. 2020, June. Increasing the space–time resolution of mapped sea surface height from altimetry. *Journal of Geophysical Research: Oceans 125*(6). https://doi.org/10.1029/2019jc015878 .

Ardhuin, F., N. Rascle, and K. Belibassakis. 2008. Explicit wave-averaged primitive equations using a generalized Lagrangian mean. *Ocean Modelling 20*(1): 35–60 .

Ardhuin, F., A. Roland, F. Dumas, A.C. Bennis, A. Sentchev, P. Forget, J. Wolf, F. Girard, P. Osuna, and M. Benoit. 2012, December. Numerical Wave Modeling in Conditions with Strong Currents: Dissipation, Refraction, and Relative Wind. *Journal of Physical Oceanography 42*(12): 2101–2120 .

Arnason, G., G. Haltiner, and M. Frawley. 1962. Higher-order geostrophic wind approximations. *Monthly Weather Review* 90: 175–185 .

Arnault, S. 1987. Tropical atlantic geostrophic currents and ship drifts. *Journal of Geophysical Research 92*(C5): 5076–5088. https://doi.org/10.1029/jc092ic05p05076 .

Atlas, R., R.N. Hoffman, S.C. Bloom, J.C. Jusem, and J. Ardizzone. 1996, May. A multiyear global surface wind velocity dataset using SSM/i wind observations. *Bulletin of the American Meteorological Society 77*(5): 869–882.

https://doi.org/10.1175/1520-0477(1996)077<0869:amgswv>2.0.co;2 .

Azevedo Correia de Souza, J.M., B. Powell, A.C. Castillo-Trujillo, and P. Flament. 2015. The vorticity balance of the ocean surface in hawaii from a regional reanalysis. *Journal of Physical Oceanography 45*(2): 424–440. https://doi.org/10.1175/JPO-D-14-0074.1 .

Bakun, A. 2006. Fronts and eddies as key structures in the habitat of marine fish larvae: opportunity, adaptive response and competitive advantage. *Scientia Marina 70*(S2): 105–122 .

Barton, E.D., M.L. Argote, J. Brown, L. Suffolk, P.M. Kosro, M. Lavin, J.M. Robles, R.L. Smith, T. na A., and H.S. Velez. 1993. Supersquirt: Dynamics of the gulf of tehuantepec, mexico. *Oceanography* 6 .

Birol, F. and C. Delebecque. 2014. Using high sampling rate (10/20 hz) altimeter data for the observation of coastal surface currents: A case study over the northwestern mediterranean sea. *Journal of Marine Systems* 129: 318–333 .

Birol, F., N. Fuller, F. Lyard, M. Cancet, F. Nino, C. Delebecque, S. Fleury, F. Toublanc, A. Melet, M. Saraceno, et al. 2017. Coastal applications from nadir altimetry: Example of the x-track regional products. *Advances in Space Research 59*(4): 936–953 .

Bleck, R. 2002, jan. An oceanic general circulation model framed in hybrid isopycnic-cartesian coordinates. *Ocean Modelling 4*(1): 55–88. https://doi.org/10.1016/s1463-5003(01)00012-9 .

Bolaños, R., P. Osuna, J. Wolf, J. Monbaliu, and A. Sánchez-Arcilla. 2011. Development of the POLCOMS–WAM current–wave model. *Ocean Modelling 36*(1–2): 102–115 .

Bolanos, R., J. Wolf, J. Brown, P. Osuna, J. Monbaliu, and A. Sanchez-Arcilla 2009. Comparison of wave-current interaction formulation using the POLCOMS-WAM wave-current model. In *Coastal Engineering 2008*, pp. 521–533.

Bonjean, F. and G.S. Lagerloef. 2002. Diagnostic model and analysis of the surface currents in the tropical pacific ocean. *Journal of Physical Oceanography 32*(10): 2938–2954 .

Breivik, Ø., P.A.E.M. Janssen, and J.R. Bidlot. 2014, September. Approximate Stokes Drift Profiles in Deep Water. *Journal of Physical Oceanography 44*(9): 2433–2445 .

Breivik, Ø., K. Mogensen, J.R. Bidlot, M. Alonso-Balmaseda, and P.A.E.M. Janssen. 2015. Surface wave effects in the NEMO ocean model: Forced and coupled experiments. *Journal of Geophysical Research: Oceans* 120: 2973–2992. https://doi.org/10.1002/2014jc010350 .

Bricheno, L.M., A. Soret, J. Wolf, O. Jorba, and J.M. Baldasano. 2013, June. Effect of high-resolution meteorological forcing on nearshore wave and current model performance. *Journal of Atmospheric and Oceanic Technology 30*(6): 1021–1037. https://doi.org/10.1175/jtech-d-12-00087.1 .

Bruinsma, S.L., C. Forste, O. Abrikosov, J.C. Marty, M.H. Rio, S. Mulet, and S. Bonvalot. 2013, July. The new ESA satellite-only gravity field model via the direct approach. *Geophysical Research Letters 40*(1): 3607–3612 .

Burchard, H., K. Bolding, and M.R. Villarreal. 1999. *GOTM, a general ocean turbulence model: theory, implementation and test cases*. Space Applications Institute.

Cancet, M., D. Griffin, M. Cahill, B. Chapron, J. Johannessen, and C. Donlon. 2019, January. Evaluation of GlobCurrent surface ocean current products: A case study in australia. *Remote Sensing of Environment* 220: 71–93. https://doi.org/10.1016/j.rse.2018.10.029 .

Chassignet, E.P., L.T. Smith, G.R. Halliwell, and R. Bleck. 2003. North Atlantic Simulations with the Hybrid Coordinate Ocean Model (HYCOM): Impact of the Vertical Coordinate Choice, Reference Pressure, and Thermobaricity. *Journal of Physical Oceanography* 33: 2504–2526 .

Chelton, D.B., M.G. Schlax, and R.M. Samelson. 2011. Global observations of nonlinear mesoscale eddies. *Progress in Oceanography 91*(2): 167–216. https://doi.org/https://doi.org/10.1016/j.pocean.2011.01.002 .

Cheney, R.E., J.G. Marsh, and B.D. Beckley. 1983. Global mesoscale variability from collinear tracks of SEASAT altimeter data. *Journal of Geophysical Research 88*(C7): 4343–4354. https://doi.org/10.1029/jc088ic07p04343 .

CMEMS. 2017. The ssalto/duacs altimeter products were produced and distributed by the copernicus marine and environment monitoring service.

de León, S.P. and C.G. Soares. 2022, November. Numerical study of the effect of current on waves in the agulhas current retroflection. *Ocean Engineering* 264: 112333. https://doi.org/10.1016/j.oceaneng.2022.112333 .

Douglass, E.M. and J.G. Richman. 2015, mar. Analysis of ageostrophy in strong surface eddies in the atlantic ocean. *Journal of Geophysical Research: Oceans 120*(3): 1490–1507. https://doi.org/10.1002/2014jc010350 .

Endlich, R.M. 1961. Computation and uses of gradient winds. *Mon. Wea. Rev* 89: 187–191 .

Feng, H., D. Vandemark, J. Levin, and J. Wilkin. 2018, August. Examining the accuracy of GlobCurrent upper ocean velocity data products on the northwestern atlantic shelf. *Remote Sensing 10*(8): 1–23. https://doi.org/10.3390/rs10081205 .

Holt, J.T. and D. James. 2001. An *s* coordinate density evolving model of the northwest European continental shelf: 1. Model description and density structure. *Journal of Geophysical Research 106*(C7): 2156–2202 .

Huang, N.E. 1971, January. Derivation of Stokes drift for a deep-water random gravity wave field. *Deep Sea Research and Oceanographic Abstracts 18*(2): 255–259 .

James, I.D. 1996. Advection scheme for shelf sea models. *Journal of Marine Systems* 8: 237–254 .

Janssen, P. 2004. *The Interaction of Ocean Waves and Wind*. Cambridge University Press.

Janssen, P.A.E.M. 1991, November. Quasi-linear Theory of Wind-Wave Generation Applied to Wave Forecasting. *Journal of Physical Oceanography 21*(11): 1631–1642 .

Kantha, L.H. and C.A. Clayson. 2004, jan. On the effect of surface gravity waves on mixing in the oceanic mixed layer. *Ocean Modelling 6*(2): 101–124. https://doi.org/10.1016/s1463-5003(02)00062-8 .

Kirby, J.T. and T.M. Chen. 1989, January. Surface waves on vertically sheared flows: Approximate dispersion relations. *Journal of Geophysical Research-Oceans 94*(C): 1013–1027 .

Komen, G.J., L. Cavaleri, M.A. Donelan, K. Hasselmann, S. Hasselmann, and P.A.E.M. Janssen. 1996, August. *Dynamics and Modelling of Ocean Waves*. Cambridge University Press.

Lagerloef, G.S.E., G.T. Mitchum, R.B. Lukas, and P.P. Niiler. 1999, October. Tropical Pacific near-surface currents estimated from altimeter, wind, and drifter data. *Journal of Geophysical Research-Oceans 104*(C): 23313–23326 .

Lewis, D. and S. Belcher. 2004, may. Time-dependent, coupled, ekman boundary layer solutions incorporating stokes drift. *Dynamics of Atmospheres and Oceans 37*(4): 313–351. https://doi.org/10.1016/j.dynatmoce.2003.11.001 .

Liang, J.H., J.C. McWilliams, J. Kurian, F. Colas, P. Wang, and Y. Uchiyama. 2012. Mesoscale variability in the northeastern tropical pacific: Forcing mechanisms and eddy properties. *Journal of Geophysical Research: Oceans 117*(C7): 1–13 .

Longuet-Higgins, M.S. 1953. Mass transport in water waves. *Philosophical Transactions of the Royal Society of London A: Mathematical, Physical and Engineering Sciences 245*(903): 535–581. https://doi.org/10.1098/rsta.1953.0006. http://rsta.royalsocietypublishing.org/content/245/903/535.full.pdf .

Lumpkin, R. and M. Pazos. 2007. Measuring surface currents with surface velocity program drifters: the instrument, its data, and some recent results. *Lagrangian analysis and prediction of coastal and ocean dynamics* 39: 67 .

Maximenko, N. and P. Niiler 2006. Mean surface circulation of the global ocean inferred from satellite altimeter and drifter data. In *Proceeding of the Symposium on 15 years of Progress in Radar Altimetry, Eur. Space Agency Spec. Publ., ESA SP*, Volume 614.

McWilliams, J.C., J.M. Restrepo, and E.M. Lane. 2004. An asymptotic theory for the interaction of waves and currents in coastal waters. *Journal of Fluid Mechanics* 511: 135–178 .

Mellor, G. 2003. The Three-Dimensional Current and Surface Wave Equations. *Journal of Physical Oceanography* 33: 1978–1989 .

Mellor, G. 2005. Some Consequences of the Three-Dimensional Current and Surface Wave Equations. *Journal of Physical Oceanography* 35: 2291 .

Morrow, R., L.L. Fu, F. Ardhuin, M. Benkiran, B. Chapron, E. Cosme, F. d'Ovidio, J.T. Farrar, S.T. Gille, G. Lapeyre, et al. 2019. Global observations of fine-scale ocean surface topography with the surface water and ocean topography (swot) mission. *Frontiers in Marine Science* 6: 1–19 .

Mulet, S., M.H. Rio, H. Etienne, C. Artana, M. Cancet, G. Dibarboure, H. Feng, R. Husson, N. Picot, C. Provost, and P.T. Strub. 2021, January. The new CNES-CLS18 global mean dynamic topography. https://doi.org/10.5194/os-2020-117 .

Müller-Karger, F.E. and C. Fuentes-Yaco. 2000. Characteristics of wind-generated rings in the eastern tropical pacific ocean. *Journal of Geophysical Research: Oceans 105*(C1): 1271–1284 .

Ocampo-Torres, F.J., H. García-Nava, R. Durazo, P. Osuna, G.M. Díaz Méndez, and H.C. Graber. 2010, November. The intOA Experiment: A Study of Ocean-Atmosphere Interactions Under Moderate to Strong Offshore Winds and

Opposing Swell Conditions in the Gulf of Tehuantepec, Mexico. *Boundary-Layer Meteorology 138*(3): 433–451 .

Osuna, P. and J. Monbaliu. 2004, December. Wave–current interaction in the Southern North Sea. *Journal of Marine Systems 52*(1-4): 65–87 .

Osuna, P. and J. Wolf 2005, June. A numerical study on the effect of wave-current interaction processes in the hydrodynamics of the Irish Sea. In *Proceedings of the 5th International Symposium Ocean Wave Measurement and Analysis*, Madrid.

Palacios, D.M. and S.J. Bograd. 2005. A census of tehuantepec and papagayo eddies in the northeastern tropical pacific. *Geophysical Research Letters 32*(23): 1–4 .

Passalacqua, G.A., J. Sheinbaum, and J.A. Martinez. 2016, may. Sea surface temperature influence on a winter cold front position and propagation: air-sea interactions of the 'nortes' winds in the gulf of mexico. *Atmospheric Science Letters 17*(5): 302–307. https://doi.org/10.1002/asl.655 .

Penven, P., I. Halo, S. Pous, and L. Marié. 2014, February. Cyclogeostrophic balance in the mozambique channel. *Journal of Geophysical Research: Oceans 119*(2): 1054–1067. https://doi.org/10.1002/2013jc009528 .

Polton, J.A., D.M. Lewis, and S.E. Belcher. 2005, apr. The role of wave-induced coriolis–stokes forcing on the wind-driven mixed layer. *Journal of Physical Oceanography 35*(4): 444–457. https://doi.org/10.1175/jpo2701.1 .

Ralph, E.A. and P.P. Niiler. 1999, sep. Wind-driven currents in the tropical pacific. *Journal of Physical Oceanography 29*(9): 2121–2129. https://doi.org/10.1175/1520-0485(1999)029<2121:wdcitt>2.0.co;2 .

Rascle, N. and F. Ardhuin. 2009, feb. Drift and mixing under the ocean surface revisited: Stratified conditions and model-data comparisons. *Journal of Geophysical Research 114*(C2): 1–17. https://doi.org/10.1029/2007jc004466 .

Rascle, N. and F. Ardhuin. 2013, October. A global wave parameter database for geophysical applications. Part 2: Model validation with improved source term parameterization. *Ocean Modelling* 70: 174–188 .

Renault, L., J.C. McWilliams, and P. Penven. 2017, 8. Modulation of the agulhas current retroflection and leakage by oceanic current interaction with the atmosphere in coupled simulations. *Journal of Physical Oceanography 47*(8): 2077–2100. https://doi.org/10.1175/jpo-d-16-0168.1 .

Renault, L., M.J. Molemaker, J.C. McWilliams, A.F. Shchepetkin, F. Lemarié, D. Chelton, S. Illig, and A. Hall. 2016, 06. Modulation of wind work

by oceanic current interaction with the atmosphere. *Journal of Physical Oceanography 46*(6): 1685–1704. https://doi.org/10.1175/jpo-d-15-0232.1 .

Reverdin, G., C. Frankignoul, E. Kestenare, and M.J. McPhaden. 1994. Seasonal variability in the surface currents of the equatorial pacific. *Journal of Geophysical Research 99*(C10): 20323–20344. https://doi.org/10.1029/94jc01477 .

Richardson, P.L. 1989. Worldwide ship drift distributions identify missing data. *Journal of Geophysical Research 94*(C5): 6169–6176. https://doi.org/10.1029/jc094ic05p06169 .

Rio, M.H. 2012, November. Use of Altimeter and Wind Data to Detect the Anomalous Loss of SVP-Type Drifter's Drogue. *Journal of Atmospheric and Oceanic Technology 29*(11): 1663–1674 .

Rio, M.H. and F. Hernandez. 2003. High-frequency response of wind-driven currents measured by drifting buoys and altimetry over the world ocean. *Journal of Geophysical Research 108*(C8): 1–19 .

Rio, M.H., S. Mulet, and N. Picot. 2014, December. Beyond GOCE for the ocean circulation estimate: Synergetic use of altimetry, gravimetry, and in situ data provides new insight into geostrophic and Ekman currents. *Geophysical Research Letters 41*(2): 8918–8925 .

Romero-Centeno, R., J. Zavala-Hidalgo, A. Gallegos, and J.J. O'Brien. 2003, August. Isthmus of tehuantepec wind climatology and ENSO signal. *Journal of Climate 16*(15): 2628–2639. https://doi.org/10.1175/1520-0442(2003)016<2628:iotwca>2.0.co;2 .

Saha, S., S. Moorthi, H.L. Pan, X. Wu, J. Wang, S. Nadiga, P. Tripp, R. Kistler, J. Woollen, D. Behringer, H. Liu, D. Stokes, R. Grumbine, G. Gayno, J. Wang, Y.T. Hou, H.Y. Chuang, H.M.H. Juang, J. Sela, M. Iredell, R. Treadon, D. Kleist, P. Van Delst, D. Keyser, J. Derber, M. Ek, J. Meng, H. Wei, R. Yang, S. Lord, H. Van Den Dool, A. Kumar, W. Wang, C. Long, M. Chelliah, Y. Xue, B. Huang, J.K. Schemm, W. Ebisuzaki, R. Lin, P. Xie, M. Chen, S. Zhou, W. Higgins, C.Z. Zou, Q. Liu, Y. Chen, Y. Han, L. Cucurull, R.W. Reynolds, G. Rutledge, and M. Goldberg. 2010, August. The NCEP Climate Forecast System Reanalysis. *Bulletin of the American Meteorological Society 91*(8): 1015–1057 .

Santiago-García, M.W., A.F. Parés-Sierra, and A. Trasviña. 2019, December. Dipole-wind interactions under gap wind jet conditions in the Gulf of Tehuantepec, Mexico: A surface drifter and satellite database analysis. *PLoS ONE 14*(12): 1–23. https://doi.org/10.1371/journal.pone.0226366 .

Schaeffer, P., Y. Faugére, J.F. Legeais, A. Ollivier, T. Guinle, and N. Picot. 2012, December. The CNES_CLS11 Global Mean Sea Surface Computed from 16 Years of Satellite Altimeter Data. *Marine Geodesy 35*(sup1): 3–19 .

Skamarock, W.C. and J.B. Klemp. 2008, mar. A time-split nonhydrostatic atmospheric model for weather research and forecasting applications. *Journal of Computational Physics 227*(7): 3465–3485. https://doi.org/10.1016/j.jcp.2007.01.037 .

Song, J.B. 2009, may. The effects of random surface waves on the steady ekman current solutions. *Deep Sea Research Part I: Oceanographic Research Papers 56*(5): 659–671. https://doi.org/10.1016/j.dsr.2008.12.014 .

Sudre, J., C. Maes, and V. Garçon. 2013, February. On the global estimates of geostrophic and Ekman surface currents. *Limnology and Oceanography: Fluids and Environments 3*(1): 1–20 .

The WAVEWATCH III ® Development Group (WW3DG). 2016. User manual and system documentation of WAVEWATCH III ® version 5.16. Technical Note 329, NOAA/NWS/NCEP/MMAB, College Park, MD, USA, 326 pp. + Appendices .

Trasviña, A. and E. Barton. 2008, May. Summer circulation in the mexican tropical pacific. *Deep Sea Research Part I: Oceanographic Research Papers 55*(5): 587–607. https://doi.org/10.1016/j.dsr.2008.02.002 .

Trasviña, A., E.D. Barton, J. Brown, H.S. Vélez, P.M. Kosro, and R.L. Smith. 1995, October. Offshore wind forcing in the Gulf of Tehuantepec, Mexico: The asymmetric circulation. *Journal of Geophysical Research-Oceans 100*(C): 20649–20663 .

Ubelmann, C., G. Dibarboure, L. Gaultier, A. Ponte, F. Ardhuin, M. Ballarotta, and Y. Faugere. 2021. Reconstructing ocean surface current combining altimetry and future spaceborne doppler data. *Journal of Geophysical Research* 126: 1–18 .

Wang, J., C. Dong, and K. Yu. 2020, April. The influences of the kuroshio on wave characteristics and wave energy distribution in the east china sea. *Deep Sea Research Part I: Oceanographic Research Papers* 158: 103228. https://doi.org/10.1016/j.dsr.2020.103228 .

Willett, C.S., R.R. Leben, and M.F. Lavín. 2006. Eddies and tropical instability waves in the eastern tropical pacific: A review. *Progress in Oceanography 69*(2-4): 218–238 .

Zamudio, L., H.E. Hurlburt, E.J. Metzger, S.L. Morey, J.J. O'Brien, C. Tilburg, and J. Zavala-Hidalgo. 2006. Interannual variability of tehuantepec eddies.

Comparing GlobCurrent dataset with numerical results from a high–resolution implementat

Journal of Geophysical Research: Oceans 111(C5): 1–21 .